



KELT-20b: A Giant Planet with a Period of $P \sim 3.5$ days Transiting the $V \sim 7.6$ Early A Star HD 185603

Michael B. Lund¹ , Joseph E. Rodriguez² , George Zhou² , B. Scott Gaudi³ , Keivan G. Stassun^{1,4} ,
 Marshall C. Johnson³ , Allyson Bieryla² , Ryan J. Oelkers¹ , Daniel J. Stevens³ , Karen A. Collins¹ , Kaloyan Penev⁵ ,
 Samuel N. Quinn² , David W. Latham² , Steven Villanueva, Jr.³ , Jason D. Eastman² , John F. Kielkopf⁶ , Thomas E. Oberst⁷ ,
 Eric L. N. Jensen⁸ , David H. Cohen⁸ , Michael D. Jorer⁹ , Denise C. Stephens⁹ , Howard Relles² , Giorgio Corfini^{10,37} ,
 Joao Gregorio¹¹ , Roberto Zambelli¹⁰ , Gilbert A. Esquerdo² , Michael L. Calkins² , Perry Berlind² , David R. Ciardi¹² ,
 Courtney Dressing^{13,14,38} , Rahul Patel¹⁵ , Patrick Gagnon^{12,16} , Erica Gonzales¹⁷ , Thomas G. Beatty^{18,19} ,
 Robert J. Siverd²⁰ , Jonathan Labadie-Bartz²¹ , Rudolf B. Kuhn^{22,23} , Knicole D. Colón²⁴ , David James²⁵ ,
 Joshua Pepper²¹ , Benjamin J. Fulton^{26,27} , Kim K. McLeod²⁸ , Christopher Stockdale²⁹ , Sebastiano Calchi Novati^{15,30} ,
 D. L. DePoy^{31,32} , Andrew Gould³ , Jennifer L. Marshall^{31,32} , Mark Trueblood³³ , Patricia Trueblood³³ ,
 John A. Johnson² , Jason Wright^{18,19} , Nate McCrady³⁴ , Robert A. Wittenmyer³⁵ , Samson A. Johnson³ ,
 Anthony Sergi³⁴ , Maurice Wilson² , and David H. Sliski³⁶ 

¹ Department of Physics and Astronomy, Vanderbilt University, Nashville, TN 37235, USA; michael.b.lund@vanderbilt.edu

² Harvard-Smithsonian Center for Astrophysics, Cambridge, MA 02138, USA

³ Department of Astronomy, The Ohio State University, Columbus, OH 43210, USA

⁴ Department of Physics, Fisk University, Nashville, TN 37208, USA

⁵ Department of Astrophysical Sciences, Princeton University, Princeton, NJ 08544, USA

⁶ Department of Physics and Astronomy, University of Louisville, Louisville, KY 40292, USA

⁷ Department of Physics, Westminster College, New Wilmington, PA 16172, USA

⁸ Department of Physics and Astronomy, Swarthmore College, Swarthmore, PA 19081, USA

⁹ Department of Physics and Astronomy, Brigham Young University, Provo, UT 84602, USA

¹⁰ Societ Astronomica Lunae, Castelnuovo Magra I-19030, Italy

¹¹ Atalaia Group & CROW Observatory, Portalegre, Portugal

¹² NASA Exoplanet Science Institute/Caltech, Pasadena, CA, USA

¹³ Division of Geological & Planetary Sciences, California Institute of Technology, Pasadena, CA 91125, USA

¹⁴ Department of Astronomy, University of California, Berkeley, CA 94720-3411, USA

¹⁵ IPAC, Mail Code 100-22, Caltech, Pasadena, CA 91125, USA

¹⁶ College of the Canyons, Santa Clarita, CA 91355, USA

¹⁷ University of California, Santa Cruz, CA, USA

¹⁸ Department of Astronomy & Astrophysics, The Pennsylvania State University, University Park, PA 16802, USA

¹⁹ Center for Exoplanets and Habitable Worlds, The Pennsylvania State University, University Park, PA 16802, USA

²⁰ Las Cumbres Observatory, Goleta, CA 93117, USA

²¹ Department of Physics, Lehigh University, Bethlehem, PA 18015, USA

²² South African Astronomical Observatory, P.O. Box 9, Observatory, 7935 Cape Town, South Africa

²³ Southern African Large Telescope, P.O. Box 9, Observatory, 7935 Cape Town, South Africa

²⁴ NASA Goddard Space Flight Center, Greenbelt, MD 20771, USA

²⁵ Astronomy Department, University of Washington, Seattle, WA 98195, USA

²⁶ Institute for Astronomy, University of Hawaii, Honolulu, HI 96822-1839, USA

²⁷ California Institute of Technology, Pasadena, CA 91125, USA

²⁸ Department of Astronomy, Wellesley College, Wellesley, MA 02481, USA

²⁹ Hazelwood Observatory, Churchill, Victoria, Australia

³⁰ Dipartimento di Fisica E. R. Caianiello, Università di Salerno, Via Giovanni Paolo II 132, I-84084 Fisciano (SA), Italy

³¹ George P. and Cynthia Woods Mitchell Institute for Fundamental Physics and Astronomy, Texas A&M University, College Station, TX 77843, USA

³² Department of Physics and Astronomy, Texas A&M University, College Station, TX 77843, USA

³³ Winer Observatory, Sonoita, AZ 85637, USA

³⁴ Department of Physics and Astronomy, University of Montana, Missoula, MT 59812, USA

³⁵ Computational Engineering and Science Research Centre, University of Southern Queensland, Toowoomba, Queensland 4350, Australia

³⁶ Department of Physics and Astronomy, University of Pennsylvania, Philadelphia, PA 19104, USA

Received 2017 July 5; revised 2017 September 14; accepted 2017 September 21; published 2017 October 20

Abstract

We report the discovery of KELT-20b, a hot Jupiter transiting a $V \sim 7.6$ early A star, HD 185603, with an orbital period of $P \simeq 3.47$ days. Archival and follow-up photometry, *Gaia* parallax, radial velocities, Doppler tomography, and AO imaging were used to confirm the planetary nature of KELT-20b and characterize the system. From global modeling we infer that KELT-20 is a rapidly rotating ($v \sin I_* \simeq 120$ km s⁻¹) A2V star with an effective temperature of $T_{\text{eff}} = 8730_{-260}^{+250}$ K, mass of $M_* = 1.76_{-0.20}^{+0.14} M_{\odot}$, radius of $R_* = 1.561_{-0.064}^{+0.058} R_{\odot}$, surface gravity of $\log g_* = 4.292_{-0.020}^{+0.017}$, and age of $\lesssim 600$ Myr. The planetary companion has a radius of $R_p = 1.735_{-0.075}^{+0.070} R_J$, a semimajor axis of $a = 0.0542_{-0.0021}^{+0.0014}$ au, and a linear ephemeris of $\text{BJD}_{\text{TDB}} = 2457503.120049 \pm 0.000190 + E(3.4741070 \pm 0.0000019)$. We place a 3σ upper limit of $\sim 3.5 M_J$ on the mass of the planet. Doppler tomographic

³⁷ This paper is dedicated to the memory of Giorgio Corfini, who passed away in 2014 December.

³⁸ NASA Sagan Fellow.

measurements indicate that the planetary orbit normal is well aligned with the projected spin axis of the star ($\lambda = 3.4 \pm 2.1$). The inclination of the star is constrained to $24.4^\circ < I_* < 155.6^\circ$, implying a three-dimensional spin-orbit alignment of $1.3^\circ < \psi < 69.8^\circ$. KELT-20b receives an insolation flux of $\sim 8 \times 10^9 \text{ erg s}^{-1} \text{ cm}^{-2}$, implying an equilibrium temperature of $\sim 2250 \text{ K}$, assuming zero albedo and complete heat redistribution. Due to the high stellar T_{eff} , KELT-20b also receives an ultraviolet (wavelength $d \leq 91.2 \text{ nm}$) insolation flux of $\sim 9.1 \times 10^4 \text{ erg s}^{-1} \text{ cm}^{-2}$, possibly indicating significant atmospheric ablation. Together with WASP-33, Kepler-13 A, HAT-P-57, KELT-17, and KELT-9, KELT-20 is the sixth A star host of a transiting giant planet, and the third-brightest host (in V) of a transiting planet.

Key words: methods: observational – planets and satellites: detection – planets and satellites: gaseous planets – stars: individual (HD 185603) – techniques: photometric – techniques: radial velocities

Supporting material: data behind figures

1. Introduction

The first surveys for exoplanets, which primarily used the radial velocity (RV) method,³⁹ focused on Sun-like (G, late F, and early K) dwarf stars. This was due to the fact that old stars with T_{eff} below the Kraft break (Kraft 1967) at $T_{\text{eff}} \simeq 6250 \text{ K}$ tend to be slowly rotating and have plentiful absorption lines, therefore enabling the submeters per second precision that was expected to be needed to detect analogs of the planets in our solar system. Stars cooler than early K also have plentiful lines, but are generally faint in the optical, where these initial surveys were carried out. Given the high-resolution ($R \gtrsim 50,000$) spectra needed to resolve the stellar spectral lines, high photon counts were difficult to acquire for cooler stars with the modest-aperture telescopes that were available at the time.

Of course, it came as a surprise when the first exoplanets discovered around main-sequence stars (Campbell et al. 1988; Latham et al. 1989; Mayor & Queloz 1995; Marcy & Butler 1996) did not resemble the planets in our solar system and typically induced much higher RV amplitudes than even our own giant planets. Indeed, the Jupiter-like planetary companion to 51 Pegasi (Mayor & Queloz 1995), which jump-started the field of exoplanets (despite not being the first exoplanet discovered), has such a short period that it creates a reflex RV amplitude on its host star of hundreds of meters per second. It is the prototypical “hot Jupiter,” a class of planets that are now known to orbit $\sim 0.5\%–1\%$ of stars (Gould et al. 2006; Howard et al. 2012; Wright et al. 2012), but whose origins and characteristics remain important topics of study.

Subsequent surveys for exoplanets, including those using the transit (Winn et al. 2010) and microlensing (Gaudi 2012) methods, began to more fully explore the planet populations of lower-mass stars, in particular around M dwarfs. The reasons for this are clear: RV, transit, and microlensing surveys are all more sensitive to planets orbiting low-mass stars (albeit for different reasons; see Wright & Gaudi 2013). For potentially habitable planets, in particular, transit surveys have an enormous advantage over other detection methods when targeting low-mass stars (Gould et al. 2003). This advantage has since been dubbed the “small star opportunity” and has been one of the many reasons that the *Kepler* (Borucki et al. 2010) mission, as well as other ground-based surveys such as M_{Earth} (Nutzman & Charbonneau 2008; Charbonneau et al. 2009; Berta et al. 2012) and TRAPPIST (Gillon et al. 2014), have been so impactful.

Indeed, in the more than 25 yr since the first confirmed exoplanets were discovered, the number of known exoplanets has increased dramatically, to almost 3500 confirmed exoplanets and an additional 2200 unconfirmed planet candidates.⁴⁰ As the field of exoplanets has developed, there have been two broad goals: determining the overall demographics of exoplanets and how these demographics depend on the properties of the planets and their host stars, and finding individual exoplanets that can be characterized in detail, in particular their atmospheres. The primary techniques for characterizing exoplanet atmospheres are transits and direct imaging. The combination of transit photometry and RV measurements can provide a planet’s radius and mass and, by extension, its density and bulk composition. Beyond this, phase curves and spectroscopy of transits and eclipses can shed light on the atmospheric properties of the system. Although planet densities can be determined even for quite faint host stars, detailed spectra and phase curves benefit greatly from having host stars that are bright (Seager & Deming 2010). Indeed, finding such bright transit hosts is one of the primary motivations of the *Transiting Exoplanet Survey* satellite (Ricker et al. 2015).

The Kilodegree Extremely Little Telescope Survey (KELT; Pepper et al. 2003, 2007, 2012) was originally designed to find transiting hot Jupiters orbiting bright ($8 \lesssim V \lesssim 10$) stars, precisely the targets best suited for follow-up and atmospheric characterization. Nevertheless, the KELT survey did not start actively vetting targets until around 2011, by which point many ground-based transit surveys had discovered a number of transiting planets orbiting moderately bright stars (Alonso et al. 2004; McCullough et al. 2005; Bakos et al. 2007; Collier Cameron et al. 2007).

Concurrently, while the overall picture of the demographics of planetary systems orbiting late F to M stars was starting to become clear, the properties of planetary systems orbiting more massive and hotter stars remained relatively murky. This was largely because the workhorse planet detection technique, RVs, begins to have difficulties achieving precisions of better than a few hundred meters per second for stars above $T_{\text{eff}} \simeq 6250 \text{ K}$, both because these stars have thin convective envelopes and so do not spin down with age owing to magnetic braking, and because they have fewer spectral lines than cooler stars. Although there were some RV surveys that targeted A and F stars, these did not result in many detections (e.g., Galland et al. 2005). Part of the difficulty with discovering planets via RVs is that one does not know a priori the ephemeris of any extant planet; as a result, one must search over many epochs and periods, thereby requiring a higher statistical significance

³⁹ While not the focus of this introduction, we would be remiss not to note the discovery of the planetary companions to the pulsar PSR 1257+12 by Wolszczan & Frail (1992).

⁴⁰ From <https://exoplanetarchive.ipac.caltech.edu/>, accessed 2017 July 3.

for detection. With transit surveys, on the other hand, the ephemeris is known precisely, and as a result only a few relatively imprecise RVs are needed to confirm the planet and measure its mass or place an upper limit on the mass that places it in the planetary mass range. Furthermore, of course, if one can measure the mass, one can measure (or place an upper limit) on the planet density.

Another avenue to studying planets orbiting more massive stars was to survey “Retired A Stars” (Johnson et al. 2007), giant stars whose progenitors were, ostensibly, A stars while on the main sequence. However, the difficulty of inferring the mass of a giant star through its observable properties led some to question whether this sample of stars was, indeed, evolved from more massive progenitors, or simply solar-mass analogs (Lloyd 2011). In recent years, several papers have provided multiple lines of evidence showing that the initial spectroscopic estimates of the masses of the “Retired A Stars” were likely generally slightly overestimated and the uncertainties in their masses likely underestimated. Indeed, it appears that the majority of the members of the “Retired A Star” sample that have accurate mass measurements (via astroseismology or transits; Johnson et al. 2014; Pepper et al. 2017; Campante et al. 2017; North et al. 2017; Stassun et al. 2017; Stello et al. 2017) appear to actually be “Retired F Stars,” i.e., more massive than the solar-type stars that dominated early RV surveys (and are therefore more massive than the Kraft break), but less massive than a zero-age main-sequence (ZAMS) A star. In retrospect, this fact should not be very surprising, as the average age of the Galactic thin disk (whose stars dominate the local solar neighborhood) is $\sim 7.4\text{--}8.2$ Gyr (Kilic et al. 2017), corresponding to the hydrogen-fusing lifetime of a ZAMS late F star.

Although (as demonstrated by the discovery announced in this paper) photometric transit surveys are certainly sensitive to hot Jupiters orbiting hotter and more massive main-sequence stars, the conventional wisdom for many years was that a positive RV detection was required to confirm a transiting planet candidate. This perception began to change around nearly the same time for independent but related reasons. First, the discovery of WASP-33b (Collier Cameron et al. 2010) demonstrated that a combination of Doppler tomography and a robust upper limit on the companion mass from RV can confirm a transiting planet. Second, the use of statistical tools by the *Kepler* mission also relaxed the perception that RV confirmation was needed to validate a planet (Torres et al. 2011; Morton 2012; Lissauer et al. 2014; although see Shporer et al. 2017, for an example of the pitfalls of statistical validation). These changes, together with the somewhat fortuitous and accidental discovery of KELT-1b (Sivverid et al. 2012), led the KELT Collaboration to pursue planets around more massive and hotter stars.

To date, including the planet KELT-20b announced here, six transiting giant planet companions to main-sequence A stars are known: WASP-33, Kepler-13 A, HAT-P-57, KELT-17, and KELT-9. A few additional companions to hot stars or remnants have been announced from the *Kepler* mission via transits, pulsation timing, or Doppler beaming (e.g., Silvotti et al. 2007, 2014; Charpinet et al. 2011; Ahlers et al. 2015; Murphy et al. 2016). Finally, several directly imaged planets orbiting young stars with $T_{\text{eff}} \gtrsim 7500$ K have been announced,⁴¹ the three

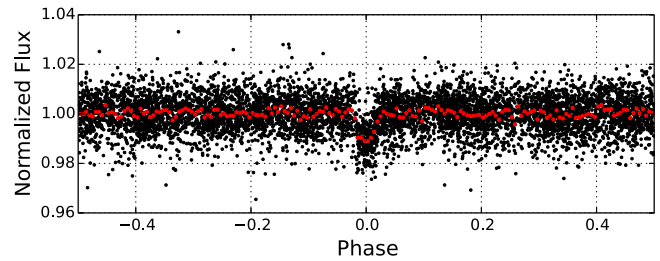


Figure 1. Discovery light curve for KELT-20b based on 6740 observations from the KELT-North telescope. The data have been phase-folded on the preliminary value for the period, 3.4739926 days. The data used to create this figure are available.

hottest of which have very large uncertainties in the masses and radii of the planets owing to the uncertain age of their parent stars, which may put them in the brown dwarf regime (Acke & van den Ancker 2006; Lafrenière et al. 2011; Carson et al. 2013). One of the advantages of discovering transiting planets orbiting bright stars is that it is possible to estimate the mass and radius of the host star to good precision (see Section 3.2).

KELT-9b is an exemplar with regard to understanding exoplanet structure around hot stars, as it is both the brightest (V magnitude of 7.55) and hottest (10,170 K) star known to host a transiting hot Jupiter and provides an excellent opportunity to characterize a planet that is receiving an extreme amount of stellar radiation (Gaudi et al. 2017). In this paper, we present the discovery and characterization of KELT-20b, a system that provides a comparison to KELT-9b of a hot Jupiter orbiting a very hot main-sequence host star. In particular, KELT-20 is the third-brightest star to host a transiting planet (in V) and the second-brightest star to host a hot Jupiter ($V = 7.58$), as well as the second-hottest host star ($T_{\text{eff}} = 8730$ K). KELT-20b is comparatively much cooler than KELT-9b, but at $T_{\text{eq}} \sim 2260$ K it is still one of the hottest exoplanets yet discovered.

2. Discovery and Follow-up Observations

2.1. Discovery

From a reduction of KELT-North field 11, KELT-20 (HD 185603) was identified as an exoplanet candidate following the same reduction and candidate selection process as described in detail in Sivverid et al. (2012). KELT-North field 11 is a $26^\circ \times 26^\circ$ area of the sky centered on $\alpha = 19^{\text{h}}27^{\text{m}}00^{\text{s}}$, $\delta = 31^\circ 39' 56''.16$ (J2000) and was observed 6740 times from UT 2007 May 30 to UT 2014 November 25. From our periodicity search using the VARTOOLS (Hartman et al. 2016) implementation of box-least-squares fitting (Kovács et al. 2002), KELT-20b was identified as a candidate with a 3.4739926-day period, 3.06 hr transit duration, and 0.81% transit depth. The phase-folded discovery light curve containing all 6740 points is shown in Figure 1. We note that KELT-20b was first identified as a candidate in a prior reduction of KELT-North field 11 using data that ended in UT 2013 June 14 (~ 700 fewer observations than are shown in Figure 1). The BLS results mentioned above are those of the initial discovery parameters. See Table 1 for the photometric and kinematic properties of KELT-20 from the literature and this work.

⁴¹ We note that the primary to the directly imaged planetary system, HR 8799 (Marois et al. 2008), is often referred to as an A star but has an effective temperature that is on the border between an A9V and F0V star (Pecaut & Mamajek 2013) and properties that are more reminiscent of a λ Boo star.

Table 1
Literature Properties for KELT-20

Parameter	Description	Value	References
Other IDs	HD 185603		
	TYC 2655-3344-1		
	2MASS J19383872+3113091		
α_{J2000}	Right Ascension (R.A.)	19 ^h 38 ^m 38 ^s .73	1
δ_{J2000}	Declination (decl.)	+31°13′09″.21	1
156.5 nm	USST (cW/m ² /nm/10 ¹²)	1.51 ± 0.17	2
196.5 nm	USST (cW/m ² /nm/10 ¹²)	3.30 ± 0.24	2
236.5 nm	USST (cW/m ² /nm/10 ¹²)	2.55 ± 0.15	2
274.0 nm	USST (cW/m ² /nm/10 ¹²)	2.27 ± 0.07	2
B_T	Tycho B_T mag	7.697 ± 0.015	3
V_T	Tycho V_T mag	7.592 ± 0.010	3
u_{Str}	$u_{Strömgren-Crawford}$ mag	9.094 ± 0.039	4
v_{Str}	$v_{Strömgren-Crawford}$ mag	7.874 ± 0.024	4
b_{Str}	$b_{Strömgren-Crawford}$ mag	7.645 ± 0.014	4
y_{Str}	$y_{Strömgren-Crawford}$ mag	7.610 ± 0.010	4
J	2MASS J mag	7.424 ± 0.024	5
H	2MASS H mag	7.446 ± 0.018	5
K_S	2MASS K_S mag	7.415 ± 0.017	5
<i>WISE1</i>	<i>WISE1</i> mag	7.394 ± 0.027	6
<i>WISE2</i>	<i>WISE2</i> mag	7.437 ± 0.020	6
<i>WISE3</i>	<i>WISE3</i> mag	7.439 ± 0.016	6
<i>WISE4</i>	<i>WISE4</i> mag	7.350 ± 0.097	6
μ_α	<i>Gaia</i> DR1 proper motion in R.A. (mas yr ⁻¹)	3.261 ± 0.026	7
μ_δ	<i>Gaia</i> DR1 proper motion in decl. (mas yr ⁻¹)	-6.041 ± 0.032	7
RV	Systemic radial velocity (km s ⁻¹)	-23.3 ± 0.3	Section 2.3
$v \sin I_*$	Projected stellar rotational velocity (km s ⁻¹)	114.0 ± 4.3	Section 4.3
Spec. type	Spectral type	A2V	Section 3.1
Age	Age (Myr)	≲600	Section 3.3
π	<i>Gaia</i> parallax (mas)	7.41 ± 0.39	5 ^a
d	<i>Gaia</i> -inferred distance (pc)	139.7±6.6	5 ^a
A_V	Visual extinction (mag)	0.07 ± 0.07	Section 3.1
Θ	Angular diameter (mas)	0.0555 ± 0.0070	Section 3.1
U	Space motion (km s ⁻¹)	1.13 ± 0.17	Section 3.4
V	Space motion (km s ⁻¹)	-8.98 ± 0.27	Section 3.4
W	Space motion (km s ⁻¹)	0.75 ± 0.18	Section 3.4

Note.

^a *Gaia* parallax after correcting for the systematic offset of -0.21 mas as described in Stassun & Torres (2016).

References. (1) van Leeuwen 2007; (2) Thompson et al. 1995; (3) Høg et al. 2000; (4) Paunzen 2015; (5) Cutri et al. 2003; (6) Cutri et al. 2012; (7) *Gaia* Collaboration et al. 2016, *Gaia* DR1; <http://gea.esac.esa.int/archive/>.

2.2. Photometric Follow-up from KELT-FUN

We obtained follow-up time-series photometry from the KELT Follow-Up Network (KELT-FUN) to better characterize the transit depth, duration, and shape, as well as to check for potential astrophysical false positives. We used a custom version of the TAPIR software package (Jensen 2013) to predict transits, and we observed 13 transits in a variety of bands between 2014 August and 2017 June, as listed in Table 2. In Figure 2 we display the photometry from all KELT-FUN observations, as well as the transit light curve when all follow-up observations are combined. Unless otherwise stated,

all data were calibrated and analyzed using the AstroImageJ package⁴² (Collins & Kielkopf 2013; Collins et al. 2017).

2.2.1. Peter van de Kamp Observatory (PvdK)

We observed KELT-20b from the Swarthmore College Peter van de Kamp Observatory (PvdK) on UT 2014 August 29 and UT 2017 May 08 in the i' band. The observations came from a 0.6 m RCOS telescope with an Apogee U16M 4K × 4K CCD, giving a 26' × 26' field of view. Using 2 × 2 binning, it has a pixel scale of 0''.76 pixel⁻¹.

2.2.2. GCO

We observed KELT-20b from Giorgio Corfini's private observatory (GCO) in Lucca, Italy, on UT 2014 September 25. The observations came from a 0.2 m Newtonian telescope with an SBIG STT-6303 ME CCD 1536 × 1024 pixel camera, having a 59' × 39' field of view and a pixel scale of 2''.3 pixel⁻¹.

2.2.3. WCO

We observed KELT-20b from the Westminster College Observatory (WCO) on UT 2015 October 06, UT 2017 May 08, and UT 2017 May 15 in the z' band. The observations came from a 0.35 m $f/11$ Celestron C14 Schmidt-Cassegrain telescope and SBIG STL-6303E CCD with a 3k × 2k array of 9 μ m pixels, having a 24' × 16' field of view and 1''.4 pixel⁻¹ image scale at 3 × 3 pixel binning.

2.2.4. Demonext

We observed KELT-20b using the DEMONEXT telescope (Villanueva et al. 2016) at Winer Observatory in Sonoita, Arizona, on UT 2016 May 21, UT 2016 June 04, and UT 2016 June 11 in the i' band. DEMONEXT is a 0.5 m PlaneWave CDK20 $f/6.8$ Corrected Dall-Kirkham Astrograph telescope with a 2048 × 2048 pixel FLI Proline CCD3041 camera, having a 30'.7 × 30'.7 field of view and a pixel scale of 0''.90 pixel⁻¹.

2.2.5. MINERVA

We observed KELT-20b using one of the MINERVA project telescopes (Swift et al. 2015) on UT 2016 November 05. MINERVA consists of four 0.7 m PlaneWave CDK-700 telescopes, located at the Fred L. Whipple Observatory on Mount Hopkins, Arizona. A single MINERVA telescope has an Andor iKON-L 2048 × 2048 camera, giving a field of view of 20'.9 × 20'.9 and a plate scale of 0''.6 pixel⁻¹.

2.2.6. MORC

We observed KELT-20b from Moore Observatory (MORC), operated by the University of Louisville, on UT 2017 May 08 in the i' band. The observations came from a 0.6 m RCOS telescope with an Apogee U16M 4K × 4K CCD, giving it a 26' × 26' and 0''.39 pixel⁻¹.

2.2.7. CDK20N

We observed KELT-20b from Moore Observatory (CDK20N), operated by the University of Louisville, on UT

⁴² <http://www.astro.louisville.edu/software/astroimagej>

Table 2
Photometric Follow-up Observations of KELT-20b

Observatory	Location	Aperture (m)	Plate Scale ("pix ⁻¹)	Date (UT)	Filter	Exposure Time (s)	Detrending Parameters ^a
PvdK	PA, USA	0.6	0.76	2014 Aug 29	i'	20	airmass, time
GCO	Lucca, Italy	0.2	2.3	2014 Sep 25	V	90	airmass
WCO	PA, USA	0.35	1.45	2015 Oct 06	z'	12	airmass
DEMONEXT	AZ, USA	0.5	0.90	2016 May 21	i'	31	None
DEMONEXT	AZ, USA	0.5	0.90	2016 Jun 04	i'	31	None
DEMONEXT	AZ, USA	0.5	0.90	2016 Jun 11	i'	31	None
MINERVA	AZ, USA	0.7	0.60	2016 Nov 05	g'	31	airmass
PvdK	PA, USA	0.6	0.76	2017 May 08	i'	20	airmass
MORC	KY, USA	0.6	0.39	2017 May 08	i'	20	airmass
CDK20N	KY, USA	0.5	0.54	2017 May 08	z'	60, 40, 30	airmass
WCO	PA, USA	0.35	1.45	2017 May 08	z'	12	airmass
WCO	PA, USA	0.35	1.45	2017 May 15	z'	12	airmass
CROW	Portalegre, Portugal	0.3	0.84	2017 Jun 11	z'	150	airmass

Note.

^a Photometric parameters allowed to vary in global fits as described in the text.

2017 May 08 in the z' band. The observations came from a 0.5 m planewave-corrected Dall-Kirkham telescope with an Apogee U16M 4K \times 4K CCD, giving it a $37' \times 37'$ field at $0''.54 \text{ pixel}^{-1}$.

2.2.8. CROW

We observed KELT-20b from Canelas Robotic Observatory (CROW) in Portalegre, Portugal, on UT 2017 June 11 in the z' band. The observations came from a 0.3 m Schmidt–Cassegrain telescope with a KAF-3200E CCD, having a $30' \times 20'$ field of view and a pixel scale of $0''.84 \text{ pixel}^{-1}$.

2.3. Spectroscopic Follow-up

We obtained a series of spectroscopic follow-up observations of KELT-20b with the Tillinghast Reflector Echelle Spectrograph (TRES) on the 1.5 m telescope at the Fred Lawrence Whipple Observatory, Mount Hopkins, Arizona, USA. TRES is a fiber-fed echelle spectrograph, with a spectral resolution of $\lambda/\Delta\lambda \sim 44,000$ and a wavelength coverage of 3900–9100 Å over the 51 orders. RVs obtained over 11 out-of-transit orbital phases were used to constrain the mass of the planetary companion. Relative RVs were derived by cross-correlating selected orders in each observed spectrum against the strongest observed spectrum of KELT-20, order by order, and this analysis excludes all orders contaminated by telluric lines or with poor signal-to-noise ratio. These “multiorder” velocities are listed in Table 3 and plotted in Figure 3. In addition, 21 in-transit observations were obtained on the night of UT 2017 April 24 to measure the Doppler tomographic transit of the planet. The analysis of these observations is described in Section 4.3.

2.4. High-contrast AO Imaging

We obtained high-resolution imaging for KELT-20 with the infrared camera PHARO behind the adaptive optics (AO) system P3K on the Palomar 200-inch Hale telescope. PHARO has a pixel scale of $0''.025 \text{ pixel}^{-1}$ (Hayward et al. 2001), and the data were obtained in the narrowband filter Br- γ on UT 2017 May 05.

The AO data were obtained in a five-point quincunx dither pattern with each dither position separated by $5''$. Each dither position was observed 3 times, each offset from the previous image by $1''$ for a total of 15 frames; the integration time per frame was 45 s. We use the dithered images to remove sky background and dark current and then align, flat-field, and stack the individual images. The PHARO AO data have a resolution of $0''.09$ (FWHM).

The sensitivity of the AO data was determined by injecting simulated sources into the final combined images with separations from the primary targets in integer multiples of the central source’s FWHM (Furlan et al. 2017). The sensitivity curve shown in Figure 4 represents the 5σ limits of the imaging data.

For KELT-20, no stellar companions were detected in the infrared adaptive optics, indicating (to the limits of the data) that the star likely has no additional components to either dilute the transit depth or confuse the determination of the origin of the transit signal (e.g., Ciardi et al. 2015).

Note that to exclude a false positive due to an eclipsing binary within the photometric aperture, we have to exclude a companion that is ~ 4.7 mag in the visual, given the transit depth of 1.3%. We can exclude companions that are brighter than ~ 7.5 mag outside of ~ 0.8 arcsec in K using the AO images. Because the contrast ratios of stars are typically maximized in the Rayleigh–Jeans tail, it is unlikely that there is a companion that is less than ~ 4.7 mag fainter in the optical in the same aperture. Thus, it is unlikely that an eclipsing binary is causing the photometric signal. Further evidence against a diluted eclipsing binary comes from the achromaticity of the transit signals. Finally, note also that the Doppler tomographic observation further eliminates the possibility of a blended eclipsing binary causing the transit signal. We discuss further evidence against a false-positive scenario in the next section.

2.5. False-positive Analysis

Despite the unusual nature of this system and the lack of a definitive measurement of the companion mass, we are confident that this system is truly a hot Jupiter transiting an early A star. The evidence for this comes from several sources that we will briefly review; however, we invite the reader to

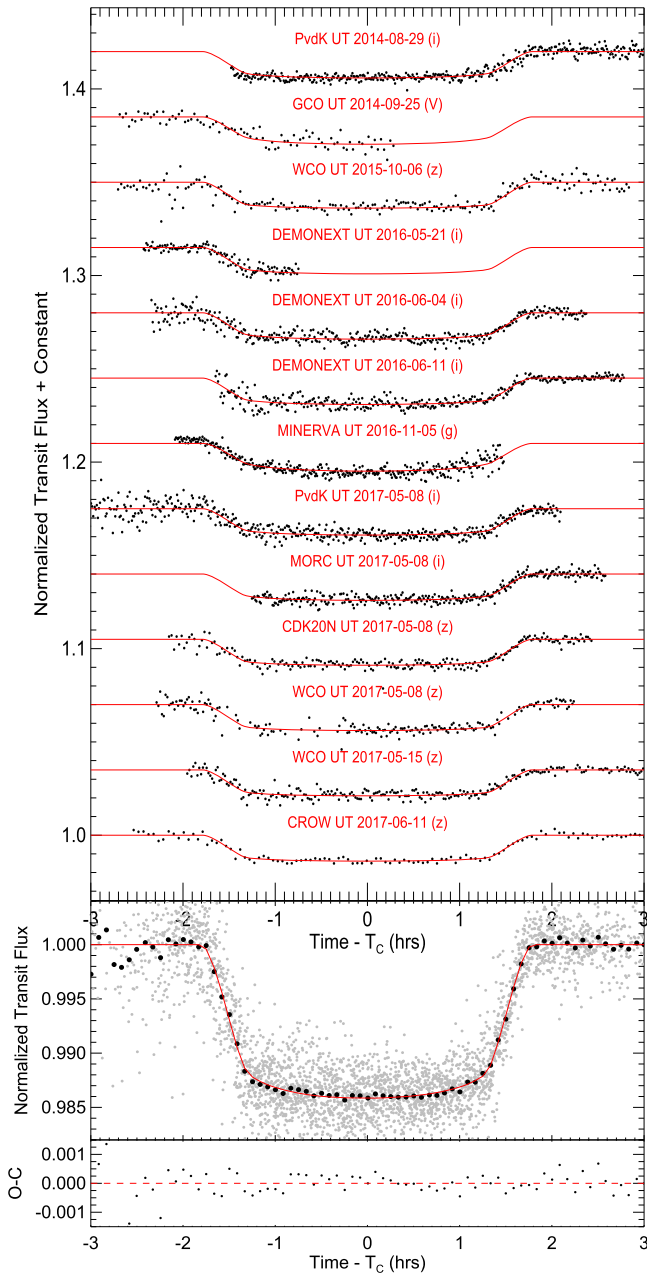


Figure 2. Top: follow-up observations of KELT-20b by the KELT Follow-Up Network. The red line represents the best-fit model for each transit. Bottom: all follow-up transits combined into one light curve (gray) and a 5-minute binned light curve (black). The red line is the combined and binned models for each transit. The data used to create this figure are available.

review Bieryla et al. (2015), Zhou et al. (2016a, 2016b), and Hartman et al. (2015) for a more detailed explanation. Of course, the first system to have been validated in this way was WASP-33b (Collier Cameron et al. 2010).

The Doppler tomographic observation eliminates the possibility of a blended eclipsing binary causing the transit signal. The line profile derived from the least-squares deconvolution shows a lack of spectroscopic companions blended with KELT-20. The spectroscopic transit is seen crossing the entirety of the rapidly rotating target star’s line profile, confirming that it is indeed orbiting KELT-20. The summed flux underneath the Doppler tomographic shadow and the

Table 3
Relative RVs for KELT-20 from TRES

BJD _{TDB}	RV (m s ⁻¹)	σ_{RV} (m s ⁻¹)
2,457,885.970564	0	397.81
2,457,890.927060	328.01	313.63
2,457,900.866772	409.74	397.81
2,457,901.852101	230.49	390.78
2,457,902.775118	759.53	355.68
2,457,903.851423	354.69	261.69
2,457,905.775362	418.55	424.11
2,457,906.798723	217.00	377.87
2,457,907.772196	447.92	347.19
2,457,908.828699	-66.87	367.83
2,457,909.823202	-263.25	287.26
2,457,910.774902	257.09	802.67

Note. The TRES RV zero-point is arbitrarily set to the first TRES value.

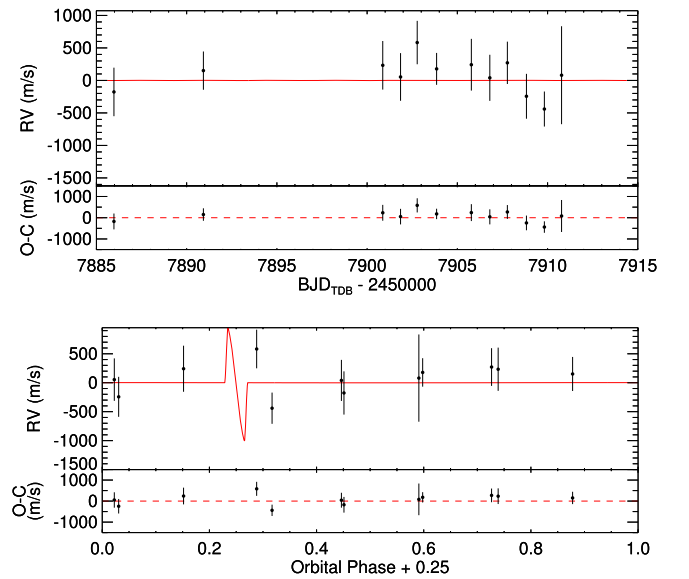


Figure 3. Top: TRES RV measurements of KELT-20b, with the best-fit model shown in red. The residuals to the fit are shown below. Bottom: RV measurements phase-folded to the global-fit-determined ephemeris. The predicted RM effect is shown at 0.25 phase. The residuals are shown below.

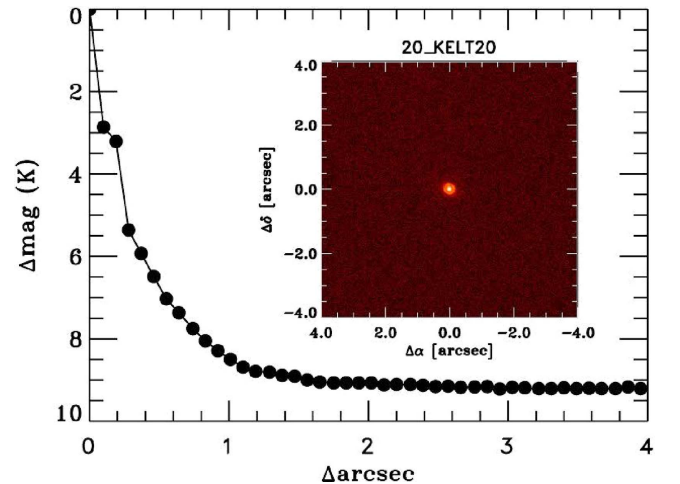


Figure 4. The 5σ contrast limit around KELT-20 in the PHARO AO data. Inset: PHARO AO image of KELT-20.

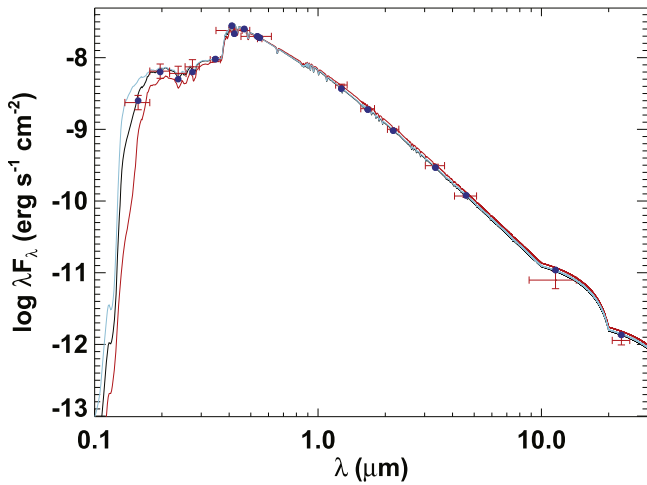


Figure 5. SED of KELT-20. The red crosses show observed broadband flux measurements, with vertical error bars representing 1σ measurement uncertainty and horizontal error bars representing the width of each bandpass. The blue dots are the predicted passband-integrated fluxes of the best-fit theoretical SED corresponding to our observed photometric bands. The best-fit Kurucz atmosphere model is shown in black; the model atmospheres representing $\pm 1\sigma$ parameters are represented in cyan and red, respectively.

distance of closest approach of the shadow from the zero velocity at the center of the predicted transit time are consistent with both the photometric transit depth and impact parameter, suggesting that the photometric transit is not diluted by background stars and is fully consistent with the spectroscopic transit. Adaptive optics observations (Section 2.4) also eliminate blended stars with $\Delta K < 7.5$ and $> 0''.6$ of KELT-20, consistent with the lack of blending in the spectroscopic analysis.

Finally, the planetary nature of KELT-20b is confirmed by the TRES RV measurements, which constrain the mass of the companion to be $\lesssim 3.5 M_{\text{Jup}}$ at 3σ significance. This eliminates the possibility that the transiting companion is a stellar-mass or brown-dwarf-mass object. As such, KELT-20b is confirmed as a planetary-mass companion transiting the rapidly rotating A star HD 185603.

Thus, we conclude that all the available evidence suggests that the most plausible interpretation is that KELT-20b is a Jupiter-size planet transiting an early A star with a projected spin-orbit alignment that is (perhaps surprisingly) well aligned (see Section 5.2.1).

3. Host Star Characterization

3.1. SED Analysis

We assembled the available broadband photometry of KELT-20 (see Table 1) in order to construct a spectral energy distribution (SED) spanning a large range of wavelengths from ~ 0.15 to $22 \mu\text{m}$ (Figure 5). We fit the SED using the model atmospheres of Kurucz (1992), the free parameters being the stellar effective temperature (T_{eff}), extinction (A_V), and a flux normalization factor (effectively the ratio of the stellar radius to the distance). The stellar surface gravity ($\log g_*$) and metallicity ($[\text{Fe}/\text{H}]$) have only a minor effect on the SED and are poorly constrained by this type of fit, so we simply adopted a solar metallicity and $\log g_* = 4.3$ (corroborated by the final global fit; see Section 4.1 and Table 4). The extinction was limited to the maximum value from the dust maps of Schlegel et al. (1998) for this line of sight, $A_V = 1.43$ mag.

The resulting best-fit parameters are $A_V = 0.07 \pm 0.07$ mag and $T_{\text{eff}} = 8800 \pm 500$ K, with a reduced chi-square of $\chi^2_\nu = 3.05$ (Figure 5). By directly integrating the (unextinguished) fitted SED model, we obtain a semi-empirical measure of the stellar bolometric flux at Earth, $F_{\text{bol}} = (2.46 \pm 0.27) \times 10^{-8}$ erg s $^{-1}$ cm $^{-2}$. From F_{bol} and T_{eff} we obtain a measure of the stellar angular radius, Θ , which in turn provides a constraint on the stellar radius via the distance from the corrected *Gaia* parallax of $R_* = 1.61 \pm 0.22 R_\odot$. This estimate of R_* is used as a constraint in the global system fit below (Section 4.1). The T_{eff} of 8800 K corresponds to an A2V-type star (Pecaut & Mamajek 2013).

3.2. Nearly Empirical Estimate of the Stellar Mass

As was originally demonstrated in the context of transiting planets by Seager & Mallén-Ornelas (2003), under the assumption that $k \equiv R_p/R_* \ll 1$, it is possible to estimate the density (ρ_*) of a host star via a measurement of the FWHM (T_{FWHM}) of the transit, the period (P), the impact parameter (b), the eccentricity, and the argument of periastron. As these quantities can be measured essentially directly (i.e., without reliance on models), one can obtain an empirical estimate of ρ_* . This can then be combined with the essentially direct estimate of R_* as determined from T_{eff} , the bolometric flux, and parallax above to estimate the stellar mass (M_*), again without reliance on theoretical models (e.g., isochrones) or externally calibrated relations (e.g., Torres et al. 2010). This technique was recently applied to all transiting planets in the first *Gaia* data release by Stassun et al. (2017).

We do not have a constraint on the eccentricity or argument of periastron, but given the short period, it is reasonable to assume that the orbit has been circularized. In the limit $e = 0$ and $k \ll 1$,

$$M_* = \left(\frac{4PR_*^3}{\pi GT_{\text{FWHM}}^3} \right) (1 - b^2)^{\frac{3}{2}}. \quad (1)$$

We adopt the estimates of P , T_{FWHM} , and b derived from global modeling (see Section 4.1) using the Yonsei–Yale (YY) isochrone-constrained circular fits given in Tables 4 and 5. We note that while these parameters formally rely on the constraints from the YY isochrones, since they are derived (almost) directly from data, their measurements are not, in fact, affected by these constraints. This can be seen by comparing the values of these parameters measured from the global modeling using the YY isochrones with those from the global modeling using the Torres relations; these parameters differ by $< 1\%$ between these two fits in all cases. Adopting the *Gaia*-inferred radius of $R_* = 1.61 \pm 0.22 R_\odot$, we find $M_* = 1.90 \pm 0.47 M_\odot$, with an uncertainty of $\sim 25\%$. We note that this uncertainty is dominated by the uncertainty in R_* .

Interestingly, this inferred mass is nearly identical to the mass inferred from the Torres-constrained global fit, and indeed the radius inferred from this global fit is nearly identical to the *Gaia*-determined radius. However, in both cases the uncertainties are somewhat smaller. This implies that the mass and radius of the host are largely determined by the direct (model-independent) constraints in the Torres-constrained global fits and completely consistent with the Torres relations. The Torres relations are therefore primarily serving to decrease the uncertainties (slightly).

Table 4
Median Values and 68% Confidence Intervals for the Physical and Orbital Parameters of the KELT-20 System

Parameter	Description (Units)	Adopted Value (YY Circular)	Value (Torres Circular)
Stellar Parameters			
M_*	Mass (M_\odot)	$1.76^{+0.14}_{-0.19}$	$1.91^{+0.22}_{-0.20}$
R_*	Radius (R_\odot)	$1.565^{+0.057}_{-0.064}$	$1.609^{+0.065}_{-0.064}$
L_*	Luminosity (L_\odot)	$12.7^{+2.2}_{-1.9}$	$13.2^{+2.3}_{-2.1}$
ρ_*	Density (cgs)	$0.641^{+0.035}_{-0.033}$	$0.646^{+0.036}_{-0.033}$
$\log g_*$	Surface gravity (cgs)	$4.290^{+0.017}_{-0.020}$	4.305 ± 0.022
T_{eff}	Effective temperature (K)	8720^{+250}_{-260}	8690^{+260}_{-280}
[Fe/H]	Metallicity	$-0.29^{+0.22}_{-0.36}$	$-0.01^{+0.50}_{-0.49}$
$v \sin I_*$	Rotational velocity (m s^{-1})	117400 ± 2900	117100 ± 2900
λ	Spin-orbit alignment (degrees)	3.1 ± 1.3	3.2 ± 1.3
$NRV_{el.W.}$	Nonrotating line width (m s^{-1})	1460^{+1300}_{-980}	1470^{+1400}_{-980}
Planet Parameters			
P	Period (days)	3.4741085 ± 0.0000019	3.4741085 ± 0.0000020
a	Semimajor axis (au)	$0.0542^{+0.0014}_{-0.0021}$	0.0557 ± 0.0020
M_P	3σ Mass Limit (M_J)	<3.382	<3.590
R_P	Radius (R_J)	$1.741^{+0.069}_{-0.074}$	1.789 ± 0.075
ρ_P	3σ Limit Density (cgs)	<0.806	<0.781
$\log g_P$	3σ Surface gravity	<3.467	<3.611
T_{eq}	Equilibrium temperature (K)	2262 ± 73	2252^{+75}_{-78}
Θ	Safronov number	$0.0048^{+0.023}_{-0.0040}$	$0.0047^{+0.022}_{-0.0039}$
$\langle F \rangle$	Incident flux ($10^9 \text{ erg s}^{-1} \text{ cm}^{-2}$)	$5.94^{+0.81}_{-0.73}$	$5.84^{+0.82}_{-0.77}$
Radial Velocity Parameters			
T_C	Time of inferior conjunction (BJD _{TDB})	$2,457,485.74965 \pm 0.00020$	$2,457,485.74965 \pm 0.00020$
K	3σ RV semi-amplitude (m s^{-1})	<311.3	<306.7
$M_P \sin i$	3σ Minimum mass (M_J)	<3.372	<3.580
M_P/M_*	3σ Mass ratio	<0.001863	<0.001788
u	RM linear limb darkening	$0.532^{+0.011}_{-0.014}$	$0.533^{+0.011}_{-0.015}$
γ_{TRES}	m s^{-1}	248^{+95}_{-96}	248 ± 96
Linear Ephemeris from Follow-up Transits			
P_{Trans}	Period (days)	3.4741070 ± 0.0000019	...
T_0	Linear ephemeris from transits (BJD _{TDB})	$2,457,503.120049 \pm 0.000190$...

Note. 3σ limits reported for KELT-20b's mass and parameters dependent on mass. The gamma velocity reported here uses an arbitrary zero-point for the multiorder relative velocities. The absolute gamma velocity based on the Mg b order analysis is $23.8 \pm 0.3 \text{ km s}^{-1}$.

Importantly, the inferred $\log g_* \simeq 4.3$ is at the higher end of what is typically expected from A stars of this T_{eff} and solar metallicity (see, e.g., Torres et al. 2010). This implies that the host is exceptionally close to (and perhaps lower than) the ZAMS for solar-metallicity stars in the parameter space of $\log g_*$ versus T_{eff} . This can be explained in several ways. First, the star could indeed have nearly solar metallicity but be very young. Second, the star could be older but have subsolar metallicity, since the ZAMS is at a lower $\log g_*$ at fixed T_{eff} for stars of lower metallicity. Finally, the measurement of R_* from the SED and parallax could have a small systematic error.

Since the Torres relations do not encode age, it is possible for this star to have a higher $\log g_*$ at solar metallicity without resulting in any tension with the empirical parameters using those relations. On the other hand, the YY isochrones do encode age, thus enforcing a maximum $\log g_*$ for a given metallicity (i.e., that of the ZAMS), and thus the inferred high $\log g_*$ disfavors this star having solar metallicity. The YY isochrone fits therefore “prefer” lower metallicities for the host

star, although we note that a solar metallicity is still allowed within $\sim 1\sigma$. The lower metallicity inferred by the YY fits also results in a somewhat smaller mass and radius than inferred from the empirical methods above and the Torres-constrained global fits.

Overall, we are agnostic about which of these three explanations are correct. Generally, we note that A stars with metallicities of $[\text{Fe}/\text{H}] \sim -0.3$ are not common, and we note that the kinematics of this star (i.e., the low UVW velocities presented in Section 3.4) support the interpretation that the star is young. Of course, we cannot rule out the simpler explanation that there are unrecognized subtle systematics affecting our inference of the radius, mass, and surface gravity of the star.

We note that a *Hipparcos* parallax also exists for this star and is $8.73 \pm 0.50 \text{ mas}$. The radius and mass inferred from the *Hipparcos* parallax are $R_* = 1.37 \pm 0.09 R_\odot$ and $M_* = 1.17 \pm 0.23 M_\odot$. These stellar parameters are inconsistent with those inferred from the *Gaia* parallax of $7.716 \pm 0.37 \text{ mas}$. In particular, as can be seen in Figures 5

Table 5
Median Values and 68% Confidence Intervals for the Physical and Orbital Parameters for the KELT-20 System

Parameter	Description (Units)	Adopted Value (YY circular)	Value (Torres circular)
R_p/R_*	Radius of the planet in stellar radii	$0.11440^{+0.00062}_{-0.00061}$	$0.11431^{+0.00064}_{-0.00062}$
a/R_*	Semimajor axis in stellar radii	7.42 ± 0.13	7.44 ± 0.13
i	Inclination (degrees)	$86.12^{+0.28}_{-0.27}$	$86.16^{+0.28}_{-0.27}$
b	Impact parameter	$0.503^{+0.025}_{-0.028}$	$0.499^{+0.026}_{-0.028}$
δ	Transit depth	0.01309 ± 0.00014	$0.01307^{+0.00015}_{-0.00014}$
T_{FWHM}	FWHM duration (days)	0.12901 ± 0.00048	0.12904 ± 0.00049
τ	Ingress/egress duration (days)	$0.01996^{+0.00080}_{-0.00077}$	$0.01984^{+0.00081}_{-0.00078}$
T_{14}	Total duration (days)	$0.14898^{+0.00091}_{-0.00088}$	$0.14889^{+0.00090}_{-0.00088}$
P_T	A priori nongrazing transit probability	$0.1193^{+0.0021}_{-0.0020}$	0.1190 ± 0.0021
$P_{T,G}$	A priori transit probability	0.1502 ± 0.0027	0.1498 ± 0.0027
$u_{1\text{Sloang}}$	Linear limb darkening	$0.3427^{+0.0091}_{-0.017}$	$0.3399^{+0.0086}_{-0.017}$
$u_{2\text{Sloang}}$	Quadratic limb darkening	$0.3362^{+0.0072}_{-0.0038}$	$0.3421^{+0.0091}_{-0.0083}$
$u_{1\text{Sloani}}$	Linear limb darkening	$0.1924^{+0.011}_{-0.0084}$	$0.186^{+0.012}_{-0.010}$
$u_{2\text{Sloani}}$	Quadratic limb darkening	$0.2442^{+0.010}_{-0.0062}$	$0.254^{+0.026}_{-0.013}$
$u_{1\text{Sloanz}}$	Linear limb darkening	$0.1229^{+0.0099}_{-0.0064}$	$0.1179^{+0.010}_{-0.0069}$
$u_{2\text{Sloanz}}$	Quadratic limb darkening	$0.2393^{+0.0099}_{-0.0080}$	$0.246^{+0.023}_{-0.012}$
u_{1V}	Linear limb darkening	$0.300^{+0.011}_{-0.015}$	$0.295^{+0.010}_{-0.015}$
u_{2V}	Quadratic limb darkening	$0.3096^{+0.0072}_{-0.0035}$	$0.3173^{+0.017}_{-0.0100}$
Secondary Eclipse			
T_S	Time of eclipse (BJD _{TDB})	$2,457,484.01259 \pm 0.00020$	$2,457,484.01260 \pm 0.00020$

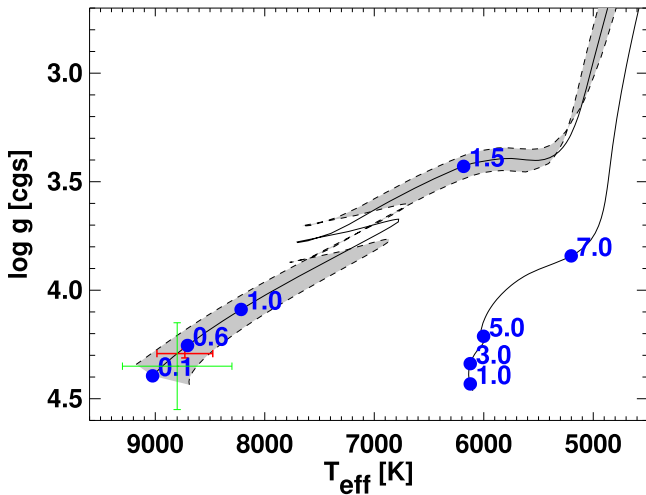


Figure 6. KELT-20 in the modified Hertzsprung–Russell diagram ($\log g_*$ vs. T_{eff}). The gray swath represents the YY evolutionary track for a star with the mass inferred from the stellar radius (via the *Gaia* parallax and transit; see Section 3.1) and 1σ error on that mass. Stellar ages (in Gyr) along the evolutionary track are indicated with blue points. The initial T_{eff} and $\log g_*$ inferred from the SED fit are represented by the green error bars; the final T_{eff} and $\log g_*$ from the global solution are represented by red error bars. For comparison, the evolutionary track for a star with the mass inferred from the *Hipparcos* parallax is also shown (see the text) and starts at a much cooler temperature.

and 6, these values are completely inconsistent with the SED (T_{eff}) or even the color of the source. We therefore reject it and adopt the *Gaia* parallax with the Stassun & Torres (2016) systematic correction. An examination of the reasons for this apparent discrepancy with the *Hipparcos* parallax is beyond the scope of this paper. Here we simply note the discrepancy and proceed with our analysis utilizing the *Gaia* parallax as a constraint on the system global solution (Section 4.1).

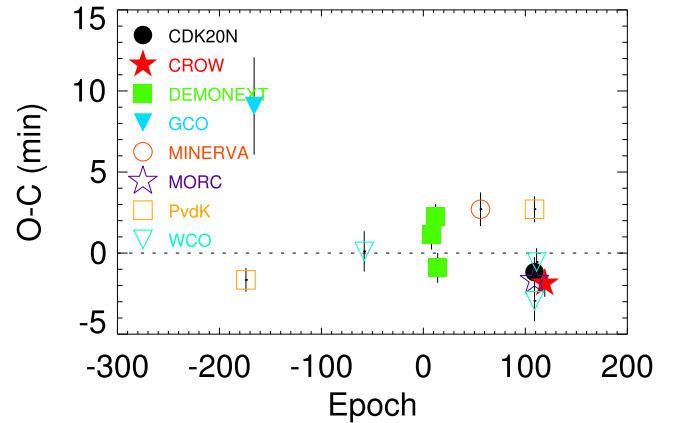


Figure 7. Transit time residuals for KELT-20b using the inferior conjunction time from the global fit to define the epoch. The data are listed in Table 6.

3.3. Evolutionary Analysis

To put the KELT-20 system in context and to provide an initial estimate of the system age, we show in Figure 6 the KELT-20 host star in the modified Hertzsprung–Russell diagram ($\log g_*$ vs. T_{eff}). Using the YY stellar evolutionary models for a star of mass $1.76 M_{\odot}$, we infer an age for KELT-20 of at most ~ 600 Myr.

3.4. Distance above the Galactic Plane and UVW Space Motion

KELT-20 is located at equatorial coordinates $\alpha = 19^{\text{h}}38^{\text{m}}38^{\text{s}}.73$ and $\delta = +31^{\circ}13'09''.21$ (J2000), corresponding to Galactic coordinates of $\ell = 65^{\circ}.8$ and $b = 4^{\circ}.6$. Given the *Gaia* distance of 139.7 ± 6.6 pc (Gaia Collaboration et al. 2016), KELT-20 lies at a galactocentric distance of roughly 8.26 kpc, assuming a distance from the Sun to the

Galactic center of $R_0 = 8.32$ kpc (Gillessen et al. 2017). KELT-20 is located ~ 10 pc above the plane, well within the Galactic scale height for A stars of ~ 50 pc (Bovy 2017).

Using the *Gaia* proper motion of $(\mu_\alpha, \mu_\delta) = (3.261 \pm 0.026, -6.041 \pm 0.032)$ mas yr $^{-1}$, the *Gaia* parallax, and the absolute RV as determined from the TRES spectroscopy of -23.8 ± 0.3 km s $^{-1}$, we find that KELT-20 has a three-dimensional Galactic space motion of $(U, V, W) = (1.14 \pm 0.17, -8.98 \pm 0.27, 0.75 \pm 0.18)$ km s $^{-1}$, where positive U is in the direction of the Galactic center, and we have adopted the Coşkunoğlu et al. (2011) determination of the solar motion with respect to the local standard of rest. These values yield a 99.5% probability that KELT-20 is a thin-disk star, according to the classification scheme of Bensby et al. (2003), as expected for its young age and early spectral type.

KELT-20 is projected against a supernova remnant, which is also visible in optical and H α survey data. This is a known supernova remnant, SNR G065.3+05.7, which is about 0.8 kpc away (Boumis et al. 2004). At a distance from *Gaia* of ~ 140 pc, this is evidently a chance projection, with KELT-20 well in front of the supernova remnant.

The line of sight toward KELT-20 in Cygnus is along the so-called Orion Spur or Orion Arm, and thus it would be expected that there would be a large population of young stars in that general direction. Most of the young associations cataloged in that direction (e.g., the Cygnus OB associations, the North America Nebula, the Pelican Nebula, NGC 6914) lie at distances of 1 kpc or more, and we were not able to locate in the literature any evidence of known star-forming regions in the vicinity of the ~ 140 pc distance to KELT-20. We also checked KELT-20's Galactic space motion against the known young moving groups, and there is no obvious match. In addition, searching *Gaia* DR1, there are no sources within 5° of KELT-20 with similar proper motion and distance.

Thus, while we cannot associate KELT-20 with any known star-forming region or known young stellar population in particular, its young age is completely plausible given its location in the Galaxy. We infer that it was likely associated with some earlier episode of star formation in our spiral arm, but its local gas and any associated young stars have since dispersed into the field population.

4. Planet Characterization

4.1. EXOFAST Global Fit

Using a heavily modified version of EXOFAST (Eastman et al. 2013), an IDL-based exoplanet fitting suite, we perform a series of global fits to determine the system parameters for KELT-20. Within the global fit, all photometric and spectroscopic observations (including the Doppler tomography signal) are simultaneously fit. EXOFAST uses either the YY stellar evolution model tracks (Demarque et al. 2004) or the Torres relations (Torres et al. 2010) to constrain the mass and radius of the host star, KELT-20. See Siverd et al. (2012) for a detailed description of the global modeling routine.

The global fit uses all follow-up raw light curves and their specified detrending parameters (shown in Table 2 as inputs). From the SED analysis (Section 3.1) we impose a prior on T_{eff} of 8800 ± 500 K. As we are unable to suitably constrain the metallicity of KELT-20 from our current observations, we set a prior on [Fe/H] of 0.0 ± 0.5 dex. We ran an initial global fit where a prior was set on the period and transit center time from

Table 6
Transit Times from KELT-20 Photometric Observations

Epoch	T_C (BJD _{TDB})	σ_{T_C} (s)	O-C (s)	O-C (σ_{T_C})	Telescope
-174	2,456,898.624275	43	-99.14	-2.27	PvdK
-166	2,456,926.424578	180	544.24	3.02	GCO
-58	2,457,301.621915	74	6.46	0.09	WCO
8	2,457,530.913718	56	70.20	1.23	DEMONEXT
12	2,457,544.810920	44	137.06	3.08	DEMONEXT
14	2,457,551.756911	55	-55.02	-1.00	DEMONEXT
56	2,457,697.671922	62	162.27	2.60	MINERVA
109	2,457,881.799595	48	162.22	3.37	PvdK
109	2,457,881.796557	49	-100.26	-2.01	MORC
109	2,457,881.796903	55	-70.37	-1.28	CDK20N
109	2,457,881.795676	75	-176.38	-2.33	WCO
111	2,457,888.745551	51	-32.88	-0.64	WCO
119	2,457,916.537500	50	-111.28	-2.21	CROW

Note. Epochs are given in orbital periods relative to the value of the inferior conjunction time from the global fit.

the analysis of the KELT-North light curve. By performing a linear fit to the transit center times, we independently determined an ephemeris for KELT-20b (See Section 4.2). We then reran the Torres and YY circular fits with a prior on the transit center time and period obtained from that analysis. The KELT-North light curve itself is not included in any of the global fits we conducted. Lastly, we use the *Gaia* parallax shown in Table 1 combined with the bolometric flux estimated from the SED fits to impose a prior on the host star's radius ($R_* = 1.610 \pm 0.216$). We performed two separate global fits where we fix the eccentricity of the planet's orbit to zero; one fit uses the YY models to determine the mass and radius of KELT-20, while the other uses the Torres relations for the same purpose. For the discussion and interpretation of the KELT-20 system, we adopt the circular YY fit. The results of both fits are shown in Tables 4 and 5.

For the output parameters shown in this paper that use solar or Jovian units, we adopt the following constants throughout: $G M_\odot = 1.3271244 \times 10^{20}$ m 3 s $^{-2}$, $R_\odot = 6.9566 \times 10^8$ m, $M_J = 0.000954638698 M_\odot$, and $R_J = 0.102792236 R_\odot$ (Standish 1995; Torres et al. 2010; Eastman et al. 2013; Prša et al. 2016).

4.2. Transit Timing Variation Analysis

We analyzed the fiducial global model transit center times of all follow-up light curves (see Table 6 and Figure 7) to search for transit timing variations (TTVs) in the KELT-20 system. Before running the global models, we confirm that all photometric time stamps are in BJD_{TDB} format (Eastman et al. 2010). To ensure the accuracy of the time stamps, follow-up observers provision telescope control computers to synchronize to a standard clock (such as the atomic clock in Boulder, CO). This synchronization is normally done periodically throughout the observing session. To assess the TTV for each light curve, we find the best linear fit to the transit center times. The resulting linear ephemeris has a reference transit center time of $T_0 = 2457503.120049 \pm 0.000190$ (BJD_{TDB}), a period of 3.4741070 ± 0.00000186 days, and a χ^2 of 60.8 with 11 degrees of freedom. We note that the large ~ 9 -minute TTV in the GCO data (Table 6) is likely the result of the partial transit coverage and systematics in the light curve (see

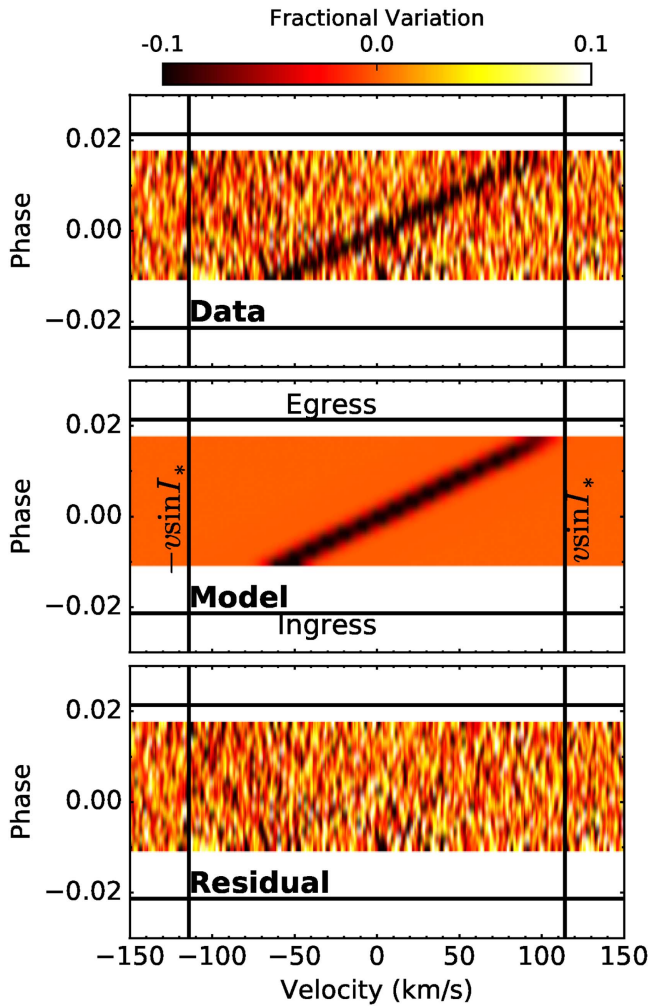


Figure 8. Doppler tomographic transit of KELT-20b, as observed by TRES on UT 2017 April 24. The top panel shows the residuals of the spectroscopic broadening kernels. The temporal axis for the spectral observations is arranged vertically, the velocity axis horizontally. The shadow cast by the planet on the rapidly rotating host star is seen moving across the star, in a spin-orbit aligned geometry, as the dark trail. The best-fit model, derived in Section 4.1, is shown in the middle panel. The vertical lines mark the boundaries of the stellar rotational profile in terms of $v \sin I_*$. The transit duration is marked with horizontal lines indicating the ingress and egress times. The bottom panel shows the residuals after the model is subtracted.

Figure 2). The largest scatter in the other light curves occurs on epoch 109 (see Table 6), where the transit was simultaneously observed by four telescopes. Using that scatter as the limit of our TTV sensitivity threshold, we find no evidence for astrophysical TTVs in our data. We therefore adopt the linear ephemeris specified above as the best predictor of future transit times from our data.

4.3. Doppler Tomographic Characterization

We obtained 21 in-transit spectroscopic observations of KELT-20b with TRES on 2017 April 24. These observations were made and processed as per Zhou et al. (2016a). For each spectrum, we derive a rotational profile via a least-squares deconvolution against a nonrotating template spectrum, as per the techniques described in Donati et al. (1997) and Collier Cameron et al. (2010). We create a median-combined rotational profile that averages out the transit signal. This median-combined rotational profile is then subtracted from each

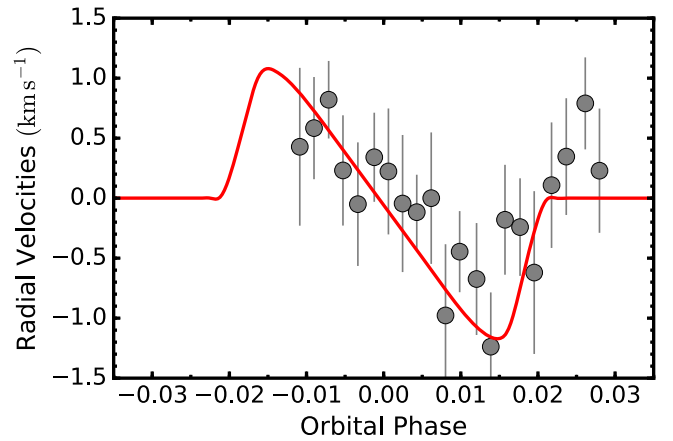


Figure 9. The Rossiter–McLaughlin effect was also detected from the same data set. We plot here the TRES multiorder RVs against the expected Rossiter–McLaughlin model, based on the best-fit geometry from our global analysis. The Rossiter–McLaughlin signal is modeled using the *ARoME* library (Boué et al. 2013). We show these data simply to confirm the consistency with the Doppler tomographic modeling; the in-transit velocities were not incorporated in the global modeling to avoid double-counting this information.

individual exposure, revealing the dark shadow of the planet transiting across the star (Figure 8). These line profile residuals are modeled in the global analysis in Section 4.1 as described in Gaudi et al. (2017). We adopt linear limb-darkening coefficients from Claret (2004) for the V band in the Doppler tomographic modeling. By modeling the rotational broadening profiles, we also measured rotational broadening parameters $v \sin I_*$ of $114.92 \pm 4.24 \text{ km s}^{-1}$ and a macroturbulence velocity of $6.08^{+4.44}_{-2.03} \text{ km s}^{-1}$. These were adopted as Gaussian priors in the global analysis in Section 4.1. In addition, we also checked the transit Doppler tomography result by deriving multiorder RVs for the same data set. These velocities also clearly show the Rossiter–McLaughlin effect (McLaughlin 1924; Rossiter 1924) consistent with the spin-orbit angle derived from the global analysis (see Figure 9).

5. Discussion

The KELT-20 system represents one of the most extreme transiting hot Jupiter systems, and indeed one of the most extreme transiting exoplanet systems, yet discovered, by several measures. The host star is both exceptionally bright ($V \sim 7.6$) and exceptionally hot ($T_{\text{eff}} \simeq 8700 \text{ K}$). It is only the sixth A star known to host a transiting giant companion. The planet itself is on a relatively short period orbit of $P \simeq 3.5$ days and thus receives an extreme amount of stellar insolation, resulting in an estimated equilibrium temperature of $\sim 2250 \text{ K}$. Because its host is an A star, it also receives a higher amount of high-energy radiation than the majority of known transiting planet systems, which may lead to significant atmospheric ablation (Murray-Clay et al. 2009).

There are two additional notable facts about the KELT-20 system. First, the host star appears to be quite young, with a main-sequence age of $\lesssim 600 \text{ Myr}$ (see Section 6). Whether or not this places interesting constraints on the migration timescale of its hot Jupiter should be considered. Second, and perhaps relatedly, the planet’s orbit normal appears to be well aligned with the spin axis of the star (see Section 5.2.1), which is generally atypical for hot Jupiters orbiting hot stars (Schlaufman 2010; Winn et al. 2010).

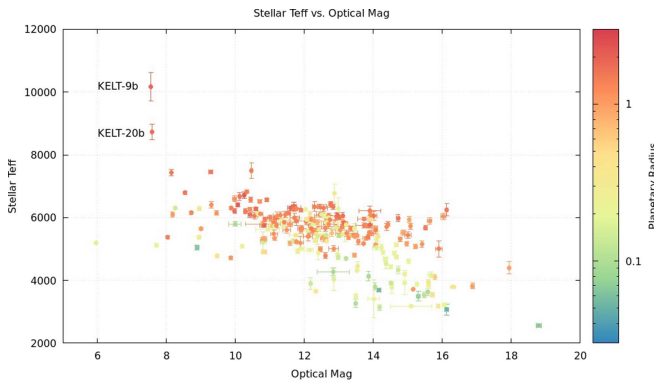


Figure 10. Population of transiting exoplanets based on the host star’s optical magnitude and effective temperature (T_{eff}), with colors indicating the radius of the planet in R_J . The bulk of these data come from the NASA Exoplanet Database (<https://exoplanetarchive.ipac.caltech.edu>), with the addition of KELT-20b to this data set. The figure was plotted using Filtergraph (Burger et al. 2013), and the data set for the plot can be found here at https://filtergraph.com/KELT20b_StellarComparison.

5.1. Prospects for Characterization

In many ways, KELT-20b appears to be quite similar to KELT-9b (Gaudi et al. 2017), albeit orbiting a slightly cooler and less massive star at a somewhat longer (~ 2.3 times) period. However, the fact that KELT-20 is nearly as bright as KELT-9 nevertheless makes the prospect for characterization of the system nearly as promising as for KELT-9b.

Figure 10 shows the host star effective temperature versus the V -band magnitude for known transiting planets. Together with 55 Cancri (Demory et al. 2011; Winn et al. 2011), KELT-9b and KELT-20b are the three brightest (in V) transiting planet hosts known, while KELT-9b and KELT-20b are the two brightest hosts of transiting hot Jupiters, which are considerably more amenable to detailed follow-up.

Figure 11 shows the primary transit depth, $\delta = (R_p/R_*)^2$, versus predicted planetary equilibrium temperature T_{eq} (assuming zero albedo and complete heat redistribution) for planets with host stars $V < 13$, color-coded by the amount of UV flux the planet receives. Although KELT-20b’s predicted equilibrium temperature is not nearly as high as KELT-9b, it is nevertheless one of the hottest dozen or so known hot Jupiters. Furthermore, its transit depth is nearly twice that of KELT-9b. Although we only have an upper limit on the mass of KELT-20b, our 3σ upper limit on the surface gravity $\log g_p$ is ~ 3.5 (cgs). We can therefore predict that the magnitude of the thermal emission spectrum, transmission spectrum, and phase curve should all be easily detectable with *Spitzer*, the *Hubble Space Telescope (HST)*, and eventually the *James Webb Space Telescope*. Indeed, the planet is sufficiently hot that secondary eclipse measurements should be possible from ground-based instruments. We also expect that, should the atmosphere be significantly ablated by the high UV flux incident on the planet, this may be detectable via *HST*.

5.2. Comparison to KELT-9 and Other A Star Hosts of Giant Transiting Planets

With a sample of six A star hosts of transiting gas giants now known, it starts to become possible to consider and compare the ensemble properties of such systems. Figure 12 shows one such comparison, namely, the location and expected future evolution of these hosts on an R_* versus

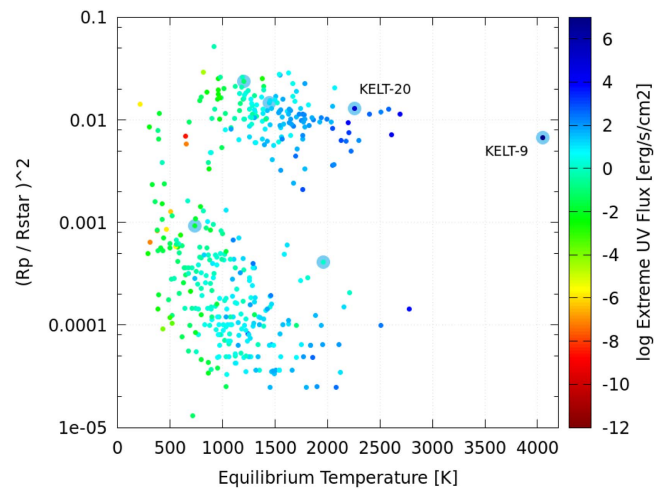


Figure 11. Depth of the transit signal, $(R_p/R_*)^2$, vs. equilibrium temperature assuming zero albedo and complete heat redistribution for known transiting planets with $V < 13$. Those with $V < 8$ are shown with large symbols. The points are color-coded by the amount of incident extreme-ultraviolet ($\lambda \leq 91.2$ nm) flux the planet receives from its parent star. In the case of the stars with $V < 8$ the color in the middle of the symbol represents this value.

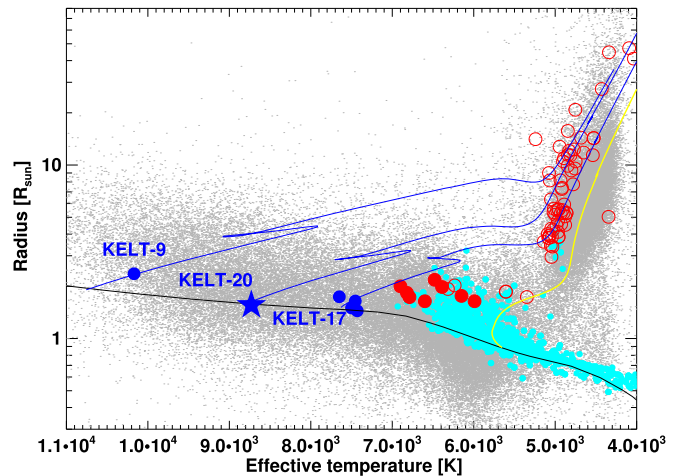


Figure 12. Radius vs. effective temperature of hosts of known planets detected by the RV (open circles) and transit methods (filled circles), as well as nearby stars in the *Hipparcos* catalog for reference (gray points). Only planet hosts with $V \leq 10$ are shown for clarity. The cyan symbols are low-mass planet hosts with $M < 1.4 M_\odot$; red symbols indicate massive planet hosts with $M_* \geq 1.4 M_\odot$. The yellow line shows the evolutionary trajectory for a solar analog ($M_* = M_\odot$ and solar metallicity), whereas the blue tracks shows the evolutionary trajectories for KELT-9, KELT-20, and KELT-17. The other three blue circles are (from left to right) Kepler-13, HAT-P-57, and WASP-33. We also show the ZAMS for solar-metallicity stars from the YY isochrones (black curve).

T_{eff} (modified Hertzsprung–Russell) diagram. We show the evolutionary tracks based on the YY isochrones for KELT-9 ($M_* \simeq 2.52 M_\odot$), KELT-20 ($M_* \simeq 1.76 M_\odot$), and KELT-17 ($M_* \simeq 1.63 M_\odot$), all assuming solar metallicity. The other three blue circles are (from left to right) Kepler-13 A ($T_{\text{eff}} \simeq 7650$ K), HAT-P-57 ($T_{\text{eff}} \simeq 7500$ K), and WASP-33 ($T_{\text{eff}} \simeq 7430$ K), all of which have quite similar T_{eff} to KELT-17 and radii and masses that differ by only $\sim 20\%$.

We note that while KELT-9, KELT-17, and Kepler-13 are somewhat evolved from the ZAMS, KELT-20 and to a lesser extent HAT-P-57 and WASP-33 appear to be on (or perhaps even slightly below) the ZAMS, indicating that they are young or (less likely) have subsolar metallicity.

5.2.1. Spin–Orbit Alignment

Doppler tomographic observations allow the measurement of the spin–orbit misalignment (λ). This, however, is merely the *sky-projected* angle between the stellar spin and planetary orbital angular momentum vectors. Measurement of the full three-dimensional spin–orbit angle (ψ) requires knowledge of the inclination of the stellar rotation axis with respect to the line of sight (I_*), which is typically difficult to measure. We do not have such a measurement of this angle for KELT-20 and so cannot directly calculate ψ .

We can, however, set limits on I_* and thus on ψ . Following Iorio (2011), we can limit I_* by requiring that the star be rotating at less than the breakup velocity. Using our measured stellar and planetary parameters, we obtain a 1σ limit of $24.4 < I_* < 155.6$. Together with our measured values of λ and i , this implies $1.3 < \psi < 69.8$ (again at 1σ).

Although the planetary orbit is well aligned if I_* is close to 90° (i.e., the stellar rotation axis is close to perpendicular to the line of sight), in which case $\psi \sim \lambda$, it may still be substantially misaligned if we are viewing the star closer to pole-on. KELT-20 has a projected rotational velocity of $v \sin I_* = 115.9 \pm 3.4$ km s $^{-1}$, which is slightly lower than the median deprojected rotational velocity of 131 km s $^{-1}$ found by Royer et al. (2007) for A2–A3 main-sequence stars. This suggests that KELT-20 is plausibly close to equator-on and approximately aligned. However, we cannot exclude the possibility that KELT-20 is rotating faster than the median for similar stars and the orbit is misaligned.

A measurement or constraint on I_* may be possible in the future via several methods. First, the detection of rotational modulation would constrain the rotation period and thus I_* ; however, this is unlikely and difficult for a hot, likely inactive A star like KELT-20. An asteroseismic measurement of the rotation rate is possible by measuring the rotational splitting of the modes. However, there is no evidence that KELT-20 is pulsating, and thus this would require long-time-baseline, very high precision space-based photometry. It may be possible to measure I_* using very high precision light curves affected by gravity darkening (Barnes 2009), or by measuring the nodal precession of the planet if it is not aligned (Johnson et al. 2015; Iorio 2016). Even in the most optimistic case, however, the precession rate will be $d\Omega/dt < 0.03$ yr $^{-1}$. This is at least an order of magnitude smaller than that measured for WASP-33b by Johnson et al. (2015) and would take several decades to give rise to a detectable change in λ or b .

Because of its larger mass and therefore more rapid evolution, KELT-20 is likely to be quite young (< 600 Myr) if it has a near-solar metallicity, as expected. This may place interesting constraints on the timescale for its migration to its current orbit. The fact that KELT-20b is one of only two hot Jupiters orbiting A-type stars that could have an aligned orbit,⁴³ as shown in Figure 13, may be particularly interesting in this regard.

5.2.2. The Past and Future Evolution of the KELT-20 System

We note that KELT-20 is a somewhat unusual system as compared to many hot Jupiters in that the spin period of the star is shorter than the orbital period of the planet. This implies that

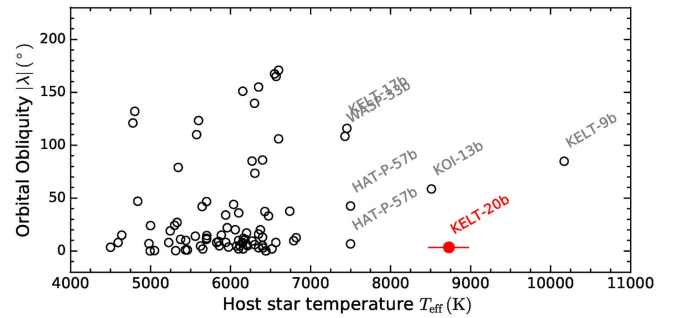


Figure 13. Projected spin–orbit angle of all transiting planets measured to date. Planets around host stars with $T_{\text{eff}} > 7000$ K are labeled. KELT-20b is only the sixth hot Jupiter found around an A star, and the first of those to be confirmed in projected spin–orbit alignment. Note that two solutions for the projected spin–orbit angle were offered by Hartman et al. (2016) for HAT-P-57b.

tides serve to increase the semimajor axis of the planet, rather than to decrease it. Furthermore, as the star has essentially no convective envelope, one would expect tides to behave quite differently than in stars with convective envelopes. Finally, the expected large oblateness of the host star may affect the efficiency and nature of tidal dissipation.

Nevertheless, we proceed to estimate the past and future orbital evolution of the system under tides. Specifically, we compute the evolution of the semimajor axis in units of the stellar radius and the evolution of the stellar insolation.

The orbital evolution of KELT-20b was calculated under the assumption of a constant phase lag, including the effect of the changing stellar radius due to stellar evolution, following Penev et al. (2014). Due to the poorly constrained efficiency of tidal dissipation in stars, we consider a wide range of dissipation parameters ($Q'_* = 10^5, 10^6, \text{ and } 10^7$), where $1/Q'_*$ is the product of the phase lag and the stellar tidal Love number. Given a dissipation parameter, the initial orbital period of the planet was chosen such that the currently observed orbital period is reproduced at an age of 480 Myr. Note that the least dissipative case considered here ($Q'_* = 10^7$) was chosen simply because it leads to very little orbital evolution and is in no way physically motivated.

Figure 14 shows the past and future evolution of the orbit of the planet relative to the stellar radius as a function of the age of the system under these assumptions. As mentioned above, unlike the majority of hot Jupiter systems, the measured $v \sin I_*$ of the host star implies that the stellar spin period is shorter than the orbital period. As a result, the typical picture of a decaying orbit is reversed and the orbit expands over time owing to tidal dissipation. Even under the fairly unrealistic value of $Q'_* \sim 10^5$, the planet will avoid engulfment by the star until well after it begins to extend up the giant branch.

Figure 14 also shows the past and future evolution of stellar incident insolation flux received by the planet. The increase in the planet’s orbit due to tides is roughly offset by the increase in the radius of the star due to stellar evolution. KELT-20b was likely always above the empirically estimated minimum insolation for inflated giant planets (Demory & Seager 2011), which is not surprising given its inferred radius of $R_p \sim 1.6 R_J$.

Note that at around 1.5 Gyr, the star will cross the Kraft break (Kraft 1967) and begin to develop a deep convective envelope. However, it is unlikely that the planet will have synchronized its period with that of the star, and so we do not expect this system to evolve into an RS CVn system (see

⁴³ Hartman et al. (2015) obtained a bimodal distribution for λ for HAT-P-57b, indicating either an aligned orbit or a prograde orbit with a substantial misalignment.

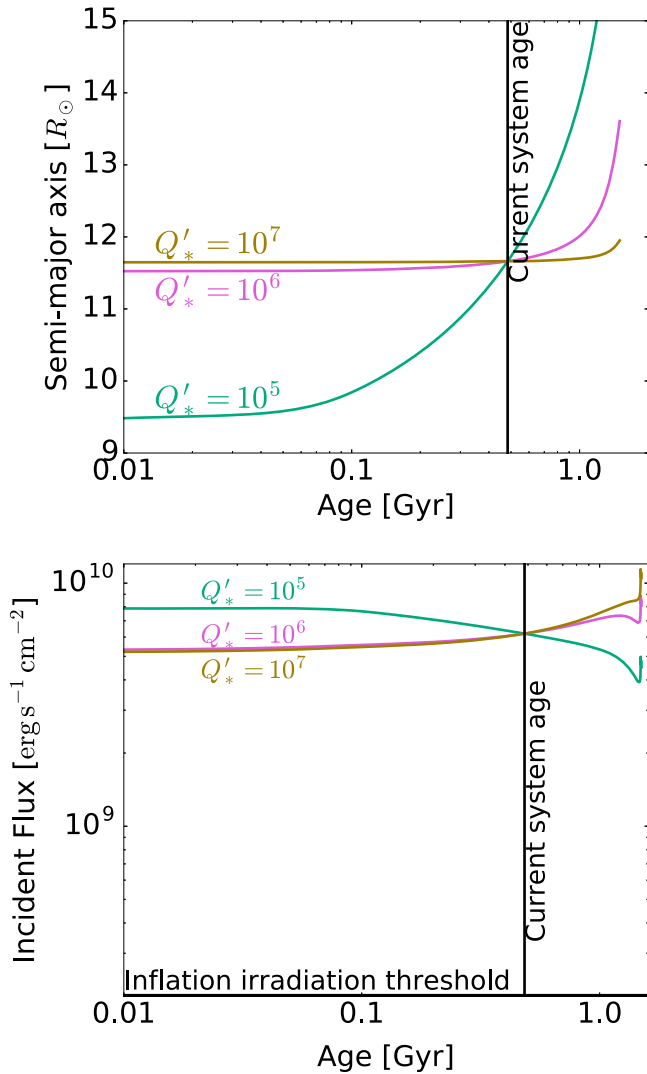


Figure 14. Top: predicted past and future tidal evolution of the semimajor axis of KELT-20b in units of the solar radius as a function of the age of the system. The current age is assumed to be roughly 480 Myr. The evolution is shown under the assumption of a constant tidal phase lag, and for various values of Q'_* , where $1/Q'_*$ is the product of the phase lag and the stellar Love number. Bottom: stellar insolation from the star received by the planet for the same assumptions as above.

Sivard et al. 2012). KELT-20 will eventually engulf its planet, but not until it has ascended the giant branch.

6. Summary

We have presented the discovery of KELT-20b, currently the third-brightest transiting planet system and the second-brightest transiting hot Jupiter system. The host star is an early A star with an effective temperature of $T_{\text{eff}} \simeq 8700$ K. The host is rapidly rotating, with $v \sin I_* \sim 116$ km s $^{-1}$. This rapid rotation made confirmation of the planet difficult using RVs, and we were only able to obtain a 3σ upper limit on the mass of the planet of $\sim 3.5 M_J$. Nevertheless, we confirm the planetary nature of the companion via Doppler tomography, which perhaps surprisingly shows that the orbit normal of the planet is well aligned with the projected spin axis of the star.

The planet has a period of ~ 3.5 days and an equilibrium temperature of ~ 2250 K, assuming zero albedo and perfect heat redistribution. With a visual magnitude of 7.6, an

exceptionally high equilibrium temperature, and a likely large-scale height, it is an excellent target for detailed follow-up and characterization of a hot Jupiter suffering from extreme stellar irradiation, particularly UV stellar irradiation.

We infer a surface gravity for the star that is surprisingly large, indicating that the star either is exceptionally young or (less likely) has a low metallicity compared to solar. We therefore encourage studies that determine whether or not the likely young age places interesting constraints on the timescale for the planet’s migration.

Finally, with a total of six A star hosts to transiting gas giants now known, we can begin to compare and contrast the ensemble properties of these systems and ultimately learn about their origins, as well as their future evolution.

We would like to thank the anonymous referee for thorough and useful report. Work performed by J.E.R. was supported by the Harvard Future Faculty Leaders Postdoctoral fellowship. D.J.S. and B.S.G. were partially supported by NSF CAREER grant AST-1056524. Work by S.V.Jr. is supported by the National Science Foundation Graduate Research Fellowship under grant no. DGE-1343012. K.G.S. acknowledges partial support from NSF PAARE grant AST-1358862. This work has made use of NASA’s Astrophysics Data System, the Extrasolar Planet Encyclopedia, the NASA Exoplanet Archive, the SIMBAD database operated at CDS, Strasbourg, France, and the VizieR catalog access tool, CDS, Strasbourg, France. We make use of Filtergraph, an online data visualization tool developed at Vanderbilt University through the Vanderbilt Initiative in Data-intensive Astrophysics (VIDA). We also used data products from the *Wide-field Infrared Survey Explorer*, which is a joint project of the University of California, Los Angeles; the Jet Propulsion Laboratory/California Institute of Technology, which is funded by the National Aeronautics and Space Administration; the Two Micron All Sky Survey, which is a joint project of the University of Massachusetts and the Infrared Processing and Analysis Center/California Institute of Technology, funded by the National Aeronautics and Space Administration and the National Science Foundation; and the European Space Agency (ESA) mission *Gaia* (<http://www.cosmos.esa.int/gaia>), processed by the *Gaia* Data Processing and Analysis Consortium (DPAC, <http://www.cosmos.esa.int/web/gaia/dpac/consortium>). Funding for the DPAC has been provided by national institutions, in particular the institutions participating in the *Gaia* Multilateral Agreement. MINERVA is a collaboration among the Harvard-Smithsonian Center for Astrophysics, Pennsylvania State University, the University of Montana, and the University of New South Wales. MINERVA is made possible by generous contributions from its collaborating institutions and the Mt. Cuba Astronomical Foundation, the David & Lucile Packard Foundation, National Aeronautics and Space Administration (EPSCOR grant NNX13AM97A), the Australian Research Council (LIEF grant LE140100050), and the National Science Foundation (grants 1516242 and 1608203).

Note added in proof. During the preparation of this paper, our team became aware of another paper by The Multi-site All-Sky CAmERA (MASCARA) Collaboration (Talens et al. 2017b) reporting the discovery of a planetary companion to the host star discussed here, HD 185603 (Talens et al. 2017a). While we assume that this planetary companion is indeed KELT-20b, no information about the analysis

procedure or any results were shared between our groups prior to the submission of both papers. We would like to thank the MASCARA Collaboration for their collegiality and willingness to work with the KELT Collaboration to coordinate our announcements of these discoveries simultaneously.

ORCID iDs

Michael B. Lund  <https://orcid.org/0000-0003-2527-1598>
 Joseph E. Rodriguez  <https://orcid.org/0000-0001-8812-0565>
 George Zhou  <https://orcid.org/0000-0002-4891-3517>
 B. Scott Gaudi  <https://orcid.org/0000-0003-0395-9869>
 Keivan G. Stassun  <https://orcid.org/0000-0002-3481-9052>
 Marshall C. Johnson  <https://orcid.org/0000-0002-5099-8185>
 Ryan J. Oelkers  <https://orcid.org/0000-0002-0582-1751>
 Karen A. Collins  <https://orcid.org/0000-0001-6588-9574>
 Kaloyan Penev  <https://orcid.org/0000-0003-4464-1371>
 Samuel N. Quinn  <https://orcid.org/0000-0002-8964-8377>
 David W. Latham  <https://orcid.org/0000-0001-9911-7388>
 Jason D. Eastman  <https://orcid.org/0000-0003-3773-5142>
 Eric L. N. Jensen  <https://orcid.org/0000-0002-4625-7333>
 Michael L. Calkins  <https://orcid.org/0000-0002-2830-5661>
 Courtney Dressing  <https://orcid.org/0000-0001-8189-0233>
 Rahul Patel  <https://orcid.org/0000-0002-5025-6827>
 Thomas G. Beatty  <https://orcid.org/0000-0002-9539-4203>
 Robert J. Siverd  <https://orcid.org/0000-0001-5016-3359>
 Jonathan Labadie-Bartz  <https://orcid.org/0000-0002-2919-6786>
 Knicole D. Colón  <https://orcid.org/0000-0001-8020-7121>
 David James  <https://orcid.org/0000-0001-5160-4486>
 Joshua Pepper  <https://orcid.org/0000-0002-3827-8417>
 Benjamin J. Fulton  <https://orcid.org/0000-0003-3504-5316>
 Kim K. McLeod  <https://orcid.org/0000-0001-9504-1486>
 Sebastiano Calchi Novati  <https://orcid.org/0000-0002-7669-1069>
 Jennifer L. Marshall  <https://orcid.org/0000-0003-0710-9474>
 Jason Wright  <https://orcid.org/0000-0001-6160-5888>
 Robert A. Wittenmyer  <https://orcid.org/0000-0001-9957-9304>

References

- Acke, B., & van den Ancker, M. E. 2006, *A&A*, 449, 267
 Ahlers, J. P., Barnes, J. W., & Barnes, R. 2015, *ApJ*, 814, 67
 Alonso, R., Brown, T. M., Torres, G., et al. 2004, *ApJL*, 613, L153
 Bakos, G. Á., Noyes, R. W., Kovács, G., et al. 2007, *ApJ*, 656, 552
 Barnes, J. W. 2009, *ApJ*, 705, 683
 Bensby, T., Feltzing, S., & Lundström, I. 2003, *A&A*, 410, 527
 Berta, Z. K., Irwin, J., Charbonneau, D., Burke, C. J., & Falco, E. E. 2012, *AJ*, 144, 145
 Bieryla, A., Collins, K., Beatty, T. G., et al. 2015, *AJ*, 150, 12
 Borucki, W. J., Koch, D., Basri, G., et al. 2010, *Sci*, 327, 977
 Boué, G., Montalto, M., Boisse, I., Oshagh, M., & Santos, N. C. 2013, *A&A*, 550, A53
 Boumis, P., Meaburn, J., López, J. A., et al. 2004, *A&A*, 424, 583
 Bovy, J. 2017, arXiv:1704.05063
 Burger, D., Stassun, K. G., Pepper, J., et al. 2013, *A&C*, 2, 40
 Campante, T. L., Veras, D., North, T. S. H., et al. 2017, *MNRAS*, 469, 1360
 Campbell, B., Walker, G. A. H., & Yang, S. 1988, *ApJ*, 331, 902
 Carson, J., Thalmann, C., Janson, M., et al. 2013, *ApJL*, 763, L32
 Charbonneau, D., Berta, Z. K., Irwin, J., et al. 2009, *Natur*, 462, 891
 Charpinet, S., Fontaine, G., Brassard, P., et al. 2011, *Natur*, 480, 496
 Ciardi, D. R., Beichman, C. A., Horch, E. P., & Howell, S. B. 2015, *ApJ*, 805, 16
 Claret, A. 2004, *A&A*, 428, 1001
 Collier Cameron, A., Bouchy, F., Hébrard, G., et al. 2007, *MNRAS*, 375, 951
 Collier Cameron, A., Guenther, E., Smalley, B., et al. 2010, *MNRAS*, 407, 507
 Collins, K., & Kielkopf, J. 2013, AstroImageJ: ImageJ for Astronomy, Astrophysics Source Code Library, ascl:1309.001
 Collins, K. A., Kielkopf, J. F., Stassun, K. G., & Hessman, F. V. 2017, *AJ*, 153, 77
 Coşkunoglu, B., Ak, S., Bilir, S., et al. 2011, *MNRAS*, 412, 1237
 Cutri, R. M., Skrutskie, M. F., van Dyk, S., et al. 2003, *yCat*, 2246, 0
 Cutri, R. M., et al. 2012, *yCat*, 2311, 0
 Demarque, P., Woo, J.-H., Kim, Y.-C., & Yi, S. K. 2004, *ApJS*, 155, 667
 Demory, B.-O., Gillon, M., Deming, D., et al. 2011, *A&A*, 533, A114
 Demory, B.-O., & Seager, S. 2011, *ApJS*, 197, 12
 Donati, J.-F., Semel, M., Carter, B. D., Rees, D. E., & Collier Cameron, A. 1997, *MNRAS*, 291, 658
 Eastman, J., Gaudi, B. S., & Agol, E. 2013, *PASP*, 125, 83
 Eastman, J., Siverd, R., & Gaudi, B. S. 2010, *PASP*, 122, 935
 Furlan, E., Ciardi, D. R., Everett, M. E., et al. 2017, *AJ*, 153, 71
 Gaia Collaboration, Brown, A. G. A., Vallenari, A., et al. 2016, arXiv:1609.04172
 Galland, F., Lagrange, A.-M., Udry, S., et al. 2005, *A&A*, 443, 337
 Gaudi, B. S. 2012, *ARA&A*, 50, 411
 Gaudi, B. S., Stassun, K. G., Collins, K. A., et al. 2017, *Natur*, 546, 514
 Gillessen, S., Plewa, P. M., Eisenhauer, F., et al. 2017, *ApJ*, 837, 30
 Gillon, M., Anderson, D. R., Collier-Cameron, A., et al. 2014, *A&A*, 562, L3
 Gould, A., Dorsher, S., Gaudi, B. S., & Udalski, A. 2006, *AcA*, 56, 1
 Gould, A., Pepper, J., & DePoy, D. L. 2003, *ApJ*, 594, 533
 Hartman, J. D., Bakos, G. Á., Bhatti, W., et al. 2016, *AJ*, 152, 182
 Hartman, J. D., Bakos, G. Á., Buchhave, L. A., et al. 2015, *AJ*, 150, 197
 Hayward, T. L., Brandl, B., Pirger, B., et al. 2001, *PASP*, 113, 105
 Høg, E., Fabricius, C., Makarov, V. V., et al. 2000, *A&A*, 355, L27
 Howard, A. W., Marcy, G. W., Bryson, S. T., et al. 2012, *ApJS*, 201, 15
 Iorio, L. 2011, *Ap&SS*, 331, 485
 Iorio, L. 2016, *MNRAS*, 455, 207
 Jensen, E. 2013, Tapir: A Web Interface for Transit/Eclipse Observability, Astrophysics Source Code Library, ascl:1306.007
 Johnson, J. A., Fischer, D. A., Marcy, G. W., et al. 2007, *ApJ*, 665, 785
 Johnson, J. A., Huber, D., Boyajian, T., et al. 2014, *ApJ*, 794, 15
 Johnson, M. C., Cochran, W. D., Collier Cameron, A., & Bayliss, D. 2015, *ApJL*, 810, L23
 Kilic, M., Munn, J. A., Harris, H. C., et al. 2017, *ApJ*, 837, 162
 Kovács, G., Zucker, S., & Mazeh, T. 2002, *A&A*, 391, 369
 Kraft, R. P. 1967, *ApJ*, 150, 551
 Kurucz, R. L. 1992, in IAU Symp. 149, The Stellar Populations of Galaxies, ed. B. Barbuy & A. Renzini (Dordrecht: Kluwer), 225
 Lafrenière, D., Jayawardhana, R., Janson, M., et al. 2011, *ApJ*, 730, 42
 Latham, D. W., Stefanik, R. P., Mazeh, T., Mayor, M., & Burki, G. 1989, *Natur*, 339, 38
 Lissauer, J. J., Marcy, G. W., Bryson, S. T., et al. 2014, *ApJ*, 784, 44
 Lloyd, J. P. 2011, *ApJL*, 739, L49
 Marcy, G. W., & Butler, R. P. 1996, *ApJL*, 464, L147
 Marois, C., Macintosh, B., Barman, T., et al. 2008, *Sci*, 322, 1348
 Mayor, M., & Queloz, D. 1995, *Natur*, 378, 355
 McCullough, P. R., Stys, J. E., Valenti, J. A., et al. 2005, *PASP*, 117, 783
 McLaughlin, D. B. 1924, *ApJ*, 60, 22
 Morton, T. D. 2012, *ApJ*, 761, 6
 Murphy, S. J., Bedding, T. R., & Shibahashi, H. 2016, *ApJL*, 827, L17
 Murray-Clay, R. A., Chiang, E. I., & Murray, N. 2009, *ApJ*, 693, 23
 North, T. S. H., Campante, T. L., Miglio, A., et al. 2017, arXiv:1708.00716
 Nutzman, P., & Charbonneau, D. 2008, *PASP*, 120, 317
 Paunzen, E. 2015, *A&A*, 580, A23
 Pécaut, M. J., & Mamajek, E. E. 2013, *ApJS*, 208, 9
 Penev, K., Zhang, M., & Jackson, B. 2014, *PASP*, 126, 553
 Pepper, J., Gould, A., & Depoy, D. L. 2003, *AcA*, 53, 213
 Pepper, J., Kuhn, R. B., Siverd, R., James, D., & Stassun, K. 2012, *PASP*, 124, 230
 Pepper, J., Pogge, R. W., DePoy, D. L., et al. 2007, *PASP*, 119, 923
 Pepper, J., Rodriguez, J. E., Collins, K. A., et al. 2017, *AJ*, 153, 215
 Prša, A., Harmanec, P., Torres, G., et al. 2016, *AJ*, 152, 41
 Ricker, G. R., Winn, J. N., Vanderspek, R., et al. 2015, *JATIS*, 1, 014003
 Rossiter, R. A. 1924, *ApJ*, 60, 15
 Royer, F., Zorec, J., & Gómez, A. E. 2007, *A&A*, 463, 671
 Schlaufman, K. C. 2010, *ApJ*, 719, 602
 Schlegel, D. J., Finkbeiner, D. P., & Davis, M. 1998, *ApJ*, 500, 525

- Seager, S., & Deming, D. 2010, *ARA&A*, 48, 631
- Seager, S., & Mallén-Ornelas, G. 2003, *ApJ*, 585, 1038
- Shporer, A., Zhou, G., Vanderburg, A., et al. 2017, *ApJL*, 847, L18
- Silvotti, R., Charpinet, S., Green, E., et al. 2014, *A&A*, 570, A130
- Silvotti, R., Schuh, S., Janulis, R., et al. 2007, *Natur*, 449, 189
- Siverd, R. J., Beatty, T. G., Pepper, J., et al. 2012, *ApJ*, 761, 123
- Standish, E. M. 1995, *HiA*, 10, 180
- Stassun, K. G., Collins, K. A., & Gaudi, B. S. 2017, *AJ*, 153, 136
- Stassun, K. G., & Torres, G. 2016, *ApJL*, 831, L6
- Stello, D., Huber, D., Grundahl, F., et al. 2017, arXiv:1708.09613
- Swift, J. J., Bottom, M., Johnson, J. A., et al. 2015, *JATIS*, 1, 027002
- Talens, G. J. J., Justesen, A. B., & Albrecht, S. 2017a, *A&A*, (arXiv:1707.01500)
- Talens, G. J. J., Spronck, J. F. P., Lesage, A.-L., et al. 2017b, *A&A*, 601, A11
- Thompson, G. I., Nandy, K., Jamar, C., et al. 1995, *yCat*, 2059, 0
- Torres, G., Andersen, J., & Giménez, A. 2010, *A&ARv*, 18, 67
- Torres, G., Fressin, F., Batalha, N. M., et al. 2011, *ApJ*, 727, 24
- van Leeuwen, F. 2007, *A&A*, 474, 653
- Villanueva, S., Eastman, J. D., Gaudi, B. S., et al. 2016, *Proc. SPIE*, 9906, 99062L
- Winn, J. N., Fabrycky, D., Albrecht, S., & Johnson, J. A. 2010, *ApJL*, 718, L145
- Winn, J. N., Matthews, J. M., Dawson, R. I., et al. 2011, *ApJL*, 737, L18
- Wolszczan, A., & Frail, D. A. 1992, *Natur*, 355, 145
- Wright, J. T., & Gaudi, B. S. 2013, in *Exoplanet Detection Methods*, ed. T. D. Oswalt, L. M. French, & P. Kalas (Netherlands: Springer), 489
- Wright, J. T., Marcy, G. W., Howard, A. W., et al. 2012, *ApJ*, 753, 160
- Zhou, G., Latham, D. W., Bieryla, A., et al. 2016a, *MNRAS*, 460, 3376
- Zhou, G., Rodriguez, J. E., Collins, K. A., et al. 2016b, *AJ*, 152, 136